Phys. Status Solidi B **250,** No. 12, 2662–2667 (2013) / **DOI** 10.1002/pssb.201300105

physica status solidi b
www.pss-b.com
basic solid state physics

In situ Raman spectroelectrochemistry of graphene oxide

Milan Bouša[*,1,2], Otakar Frank[,1], Ivan Jirka[1], and Ladislav Kavan[1,2]**

[1] Department of Electrochemical Materials, J. Heyrovský Institute of Physical Chemistry of the AS CR, v.v.i., Dolejškova 3, 18223 Prague 8, Czech Republic
[2] Faculty of Science, Department of Inorganic Chemistry, Charles University, 12840 Prague 2, Czech Republic

Received 29 April 2013, revised 22 August 2013, accepted 7 October 2013
Published online 18 November 2013

Keywords electrochemical reduction, graphene oxide, Raman spectroscopy, X-ray photoelectron spectroscopy

[*] Corresponding author: e-mail: milan.bousa@jh-inst.cas.cz, Phone: +420 266053955, Fax: +420 286582307
[**] e-mail: otakar.frank@jh-inst.cas.cz, Phone: +420 266053446, Fax: +420 286582307

Electrochemical reduction of few-layer graphene oxide (FLGO) is a simple method for a partial restoration of sp^2 network of the graphitic planes damaged by the previous oxidation/exfoliation process, and it is especially interesting for the *in situ* activation of FLGO in applications for energy conversion and storage. We present a detailed study of the structural evolution of FLGO and also non-oxidized graphene nanoplatelets (GNP) during electrochemical treatment. Two phases of the process can be traced tentatively in the case of FLGO by *ex situ* X-ray photoelectron spectroscopy and both *ex situ* and *in situ* Raman spectroscopy. The first phase is irreversible and dominated by a fast removal of oxygen-bearing functional groups accompanied by a structural ordering, while the second phase shows only a slow irreversible progressive reduction and the major changes in the Raman spectra caused by lattice expansion/contraction upon doping or a mild oxidation/reduction are reversible this time. In GNP, no irreversible reduction is observed, i.e. the first phase is absent, leaving only the reversible variations traceable in the Raman spectra.

© 2013 WILEY-VCH Verlag GmbH & Co. KGaA, Weinheim

1 Introduction Graphene oxide (GO) [1] and its reduced counterpart (RGO) [2] belong nowadays to promising materials with prospective or even existing applications in construction, energy storage and conversion, catalysis, and many others [3–6]. GO is usually produced from powdered graphite through a strong oxidative process, following e.g., the protocol introduced by Hummers and Offeman [7]. The oxidation results in graphite chunks heavily decorated by oxygen-containing groups both in- and out-of-plane of the graphitic layer, which not only expand the interlayer distance but also make the product hydrophilic [1, 5]. After a moderate ultrasonic agitation, a stable aqueous dispersion of few-layered graphene oxide (FLGO) is obtained. The exact oxidation degree of GO depends on the particular conditions used, but in general the sp^2 nature of the precursor is highly distorted with sheet conductivities dropping to 10^{-5} S cm^{-1} [8]. A lot of effort has been put recently into searching the ways how to restore the original structure of graphene layers and thus their exceptional properties [4, 5, 8]. Out of the most explored, we may name thermal treatment [8–10], chemical reduction using hydrazine or other reductants (see e.g., [2, 8, 10]), or electrochemical reduction [11–19]. However, none of the so far presented methods is able to fully heal the defects caused by oxidation. The best results are achieved by heating in vacuum, inert or reducing atmospheres at temperatures at least 1000 °C giving sheet conductivity up to 10^3 S cm^{-1}, which is still several times smaller than the conductivity of pristine graphene [20]. The mechanisms of GO reduction by the two mentioned methods – i.e., thermal and chemical, are investigated with focus on their improvement and selectivity [4, 5]. However, the electrochemical reduction of GO is less understood at the moment. The spontaneous self-activation of GO through its *in situ* electrochemical reduction might be applicable in solar cells [6], batteries [13], and capacitors [17].

In the presented work, we probed GO and graphene nanoplatelets (GNP) by *ex situ* Raman spectroscopy and *in situ* Raman spectroelectrochemistry during voltammetric cycling and also potentiostatic charging both under reductive and mildly oxidative potentials. The obtained results are discussed together with surface analysis by *ex situ* X-ray

© 2013 WILEY-VCH Verlag GmbH & Co. KGaA, Weinheim

photoelectron spectroscopy (XPS). General trends were revealed in narrowing of linewidths of the Raman bands. On the other hand, the interpretation of other observed parameters of the Raman spectra needs to be done carefully to avoid misleading conclusions about the structure of the product.

2 Experimental section

2.1 Preparation of electrodes Few-Layered Graphene Oxide (FLGO, Cheap Tubes, Inc., USA, 2–4 layers, >99 wt% purity, thickness <3 nm, average dimensions of individual flakes range from 300 to 800 nm) and Graphene NanoPlatelets (GNP, Cheap Tubes, Inc., average diameter 5μm, >97% purity, thickness <3 nm) were both suspended in deionized water (1 mg mL^{-1}) or isopropanol, respectively. The suspension was evaporated to dryness at room temperature. For experiments in aprotic electrolyte solutions, the material was mixed with 5 wt% of polyvinylidene fluoride (PVDF) dissolved in *N*-methyl-2-pyrrolidone (NMP), and doctor bladed onto F-doped SnO_2 conducting glass support (FTO). The electrodes were dried at 100 °C in vacuum. The projected area of the electrode film was 0.8–1.2 cm^2. Electrodes for spectroelectrochemistry containing only FLGO or GNP were prepared by repeated dipping of platinum mesh (99.9% purity), into the respective suspension.

GNP or FLGO samples for XPS measurements were deposited onto a gold foil (0.1 mm thickness, 99.95% purity) from the dispersions in isopropanol or water, respectively. The covered area was 0.8 cm^2. Samples were evaporated at 70 °C in vacuum.

2.2 Methods Electrochemical measurements were carried out in a one-compartment cell using an Autolab Pgstat-30 (Ecochemie) controlled by GPES-4 or Nova software. For experiments in aprotic electrolyte solutions, 1 mol L^{-1} $LiPF_6$ in ethylene carbonate + dimethylcarbonate (EC/DMC; 1/1; w/w) was used. The reference and counter electrodes were from Li-metal. Measurements were carried out in a glove box under Ar atmosphere. During the spectroelectrochemistry in aqueous electrolytes a three-electrode cell with a silver wire as pseudoreference and platinum wire as counter electrodes was used with 1 M KOH electrolyte. The sample of FLGO or GNP was deposited on a Pt mesh as a working electrode.

Raman spectra were measured by Labram HR spectrometer (Horiba Jobin-Yvon) interfaced to an Olympus BX-41 microscope. Spectroelectrochemical studies used 514 nm (2.41 eV) excitation, while 514 or 633 nm (1.96 eV) lasers were used for *ex situ* measurements. The Raman spectrometer was calibrated by the F_{1g} line of Si at 520.5 cm^{-1}. The D and G(+D′) peaks were fitted by Lorentzian and Breit–Wigner–Fano lineshapes, respectively, according to [21].

The XPS experiments were carried out using an ESCA 3 Mk 2 spectrometer (VG) with a hemispherical analyzer in fixed transmission mode, using a band pass energy of 20 eV. The photoelectrons were excited by the Al $K\alpha_{1,2}$ radiation (1486.6 eV). The pressure during an experiment was of the order of $\approx 10^{-9}$ mbar. Binding energies E_b were calibrated using the E_b of the C1s photoelectron line of HOPG (284.4 eV) [22]. A damped nonlinear least-square fitting procedure was used to distinguish partially resolved lines in O 1s, Ti 2p, Nb 3d, and C 1s in the photoelectron spectra using XPSPEAK 4.1 software. The spectra were approximated by a weighted sum of Gaussian and Lorentzian functions.

3 Results and discussion

Redox behavior of both GNP and FLGO was studied by cyclic voltammetry in aqueous as well as organic solvents. Figure 1 shows an evolution of voltammograms of GNP and FLGO during successive cycles in an aprotic environment at a constant scan rate 1 mV s^{-1}. A clear reduction peak can be observed in the first cycle of FLGO at 2.3 V versus Li/Li^+. The peak quickly vanishes in a few following cycles and is completely irreversible. However, ongoing changes in the material can be traced even further by a gradual decrease of the current

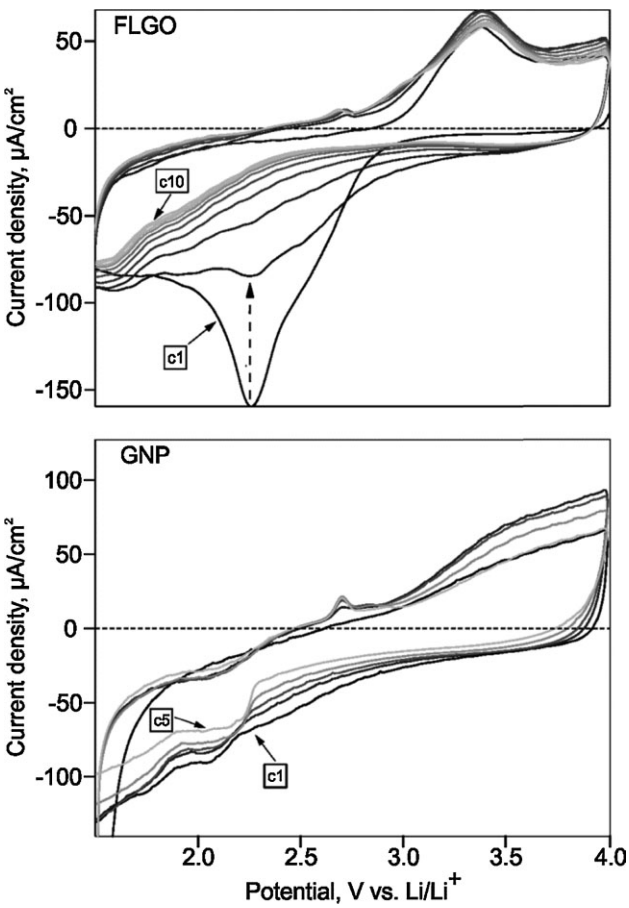

Figure 1 Cyclic voltammograms of FLGO (10 scans) and GNP (5 scans) electrode at a scan rate of 1 mV s^{-1} in 1 M $LiPF_6$ in EC/DMC. The increase in scan number is indicated by a progressive lightening of the line. First and tenth (fifth) voltammograms are labeled for FLGO (GNP). The vertical dashed arrow in the top graph marks the reduction peak of FLGO.

© 2013 WILEY-VCH Verlag GmbH & Co. KGaA, Weinheim

densities on the reduction side. These changes are reflected also on the oxidation side, indicating a lower overall electrochemical activity in the tested potential window (1.5–4 V vs. Li/Li^+) caused by the loss of functional groups with lower overpotentials. The cyclic behavior is essentially similar for both media (not shown for an aqueous electrolyte here), which has been documented in recent work [12]. In the case of GNP, the main difference consists in the absence of the pronounced reduction peak, hence in the absence of easily reduced oxidic functional groups.

A more detailed insight into the changes caused by the above described electrochemical cycling is provided by XPS. Both carbon and oxygen 1s core level spectra are shown in Fig. 2.

The photoelectron spectra of GNP correspond to microcrystalline graphite [22]. The graphitic C1s peak is asymmetric towards higher binding energies, with the main C–C peak at 284.6 eV being accompanied by a pronounced shoulder peak at ~285.7 eV originating from various defects stemming from non-ideal sp^2 C–C bonds or C–H bonds [22, 23]. A weak band at ~288 eV corresponds to various oxygen bonded carbon atoms. It should be noted here, that XPS fitting was done mainly to illustrate general trends rather than to provide precise quantitative data, which are always burdened by the impossibility to deconvolute heavily overlapping peaks. Application of several peaks with symmetrical lineshapes for the states related with sp^2 hybridization instead of only one asymmetrical is in line with findings of others [24]. For this reason we chose to include two peaks for carbon–oxygen functionalities in C1s spectra of FLGO – one for C–O (in hydroxyl and epoxy groups) at ~286.7 eV, and one for CO and OC–O^- at ~288.2 eV. In the latter one, two types of groups are often further simulated in the literature (CO at 287.5 eV and OC–O^- at 290.6 eV) [2, 8]. The basic fitting parameters are evaluated in Table 1. We can trace a gradual increase of the C/O ratio with prolonged cycling of FLGO, however, the change is much more pronounced in the first 10 cycles than in the following 60. On the other hand, the fraction of oxidized carbon atoms diminishes appreciably even in the later cycles. We ascribe this discrepancy (i) to selective reduction of functional groups containing less oxygen (like C–O–C) and/or (ii) to accumulation of CO_2 evolved during the reactions [8, 25]. The evolution of CO_2 is probably reflected also in the O1s spectra (insets in Fig. 2), which causes the relative increase of the peak attributed to the CO (and OC–O^-) at ~531.1 eV compared to the peak attributed to C–O at ~532.6 eV [8, 25].

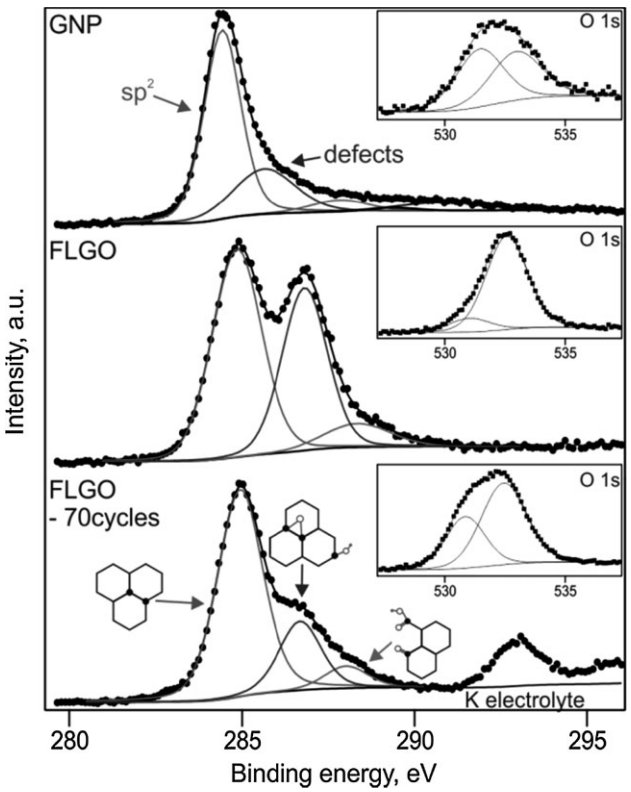

Figure 2 C1s XPS spectra of graphene nanoplatelets and graphene oxide before and after electrochemical cycling. The corresponding O1s spectra are plotted in insets. Presumed graphene-like structures of carbon atoms in different chemical states label the peaks in FLGO. Signs of K-contamination from electrolyte are visible in the bottom spectrum.

Table 1 Overall C/O stoichiometry, fraction of total oxidized carbon atoms (C^{ox}/C) and fraction of oxygen in the oxidized phase (O/C^{ox}) calculated from XPS peak areas in the series of investigated samples.

sample	C/O	C^{ox}/C	O/C^{ox}
FLGO raw	2.75	0.87	0.42
FLGO 10 cycles	3.55	0.62	0.46
FLGO 70 cycles	3.72	0.41	0.65
GNP	13.89	0.09	0.79

Raman spectroscopy represents the mostly employed characterization method for carbonaceous materials. In pristine graphene, Raman spectroscopy can distinguish the number of layers [26], their doping [27, 28] or strain [29]. In defective sp^2-based materials, Raman spectra can provide qualitative information on the disorder degree [21, 30], and with some caution even quantitative data on the crystallite sizes can be obtained [21, 30–34].

Figure 3 shows *ex situ* Raman spectra of FLGO electrodes before and after chronoamperometric cycling. We might observe all characteristic Raman features of disordered carbonaceous materials: broad and intense D band at ~1350 cm^{-1}, and overlapping (but discernible in this case) G and D′ bands at ~1580 and ~1615 cm^{-1}, respectively. The inset in Fig. 3 shows the 2D (or G′), D + D′ and 2G bands at ~2680, 2950, and 3250 cm^{-1}, respectively. The G band originates from a conventional first order Raman scattering process and corresponds to the in-plane, zone center, doubly degenerate phonon mode (transverse (TO) and longitudinal (LO) optical) with E_{2g} symmetry [30]. The D and 2D modes come from a second-order double and triple resonant process, respectively, between non-equivalent

© 2013 WILEY-VCH Verlag GmbH & Co. KGaA, Weinheim

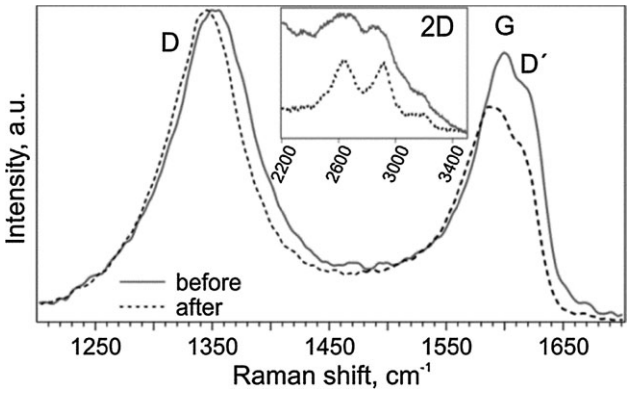

Figure 3 *Ex situ* Raman spectra of FLGO before (solid line) and after (dashed line) chronoamperometric cycling (50 cycles). The inset shows Raman 2D bands. The spectra are normalized to the D band intensity. Excitation wavelength is 633 nm.

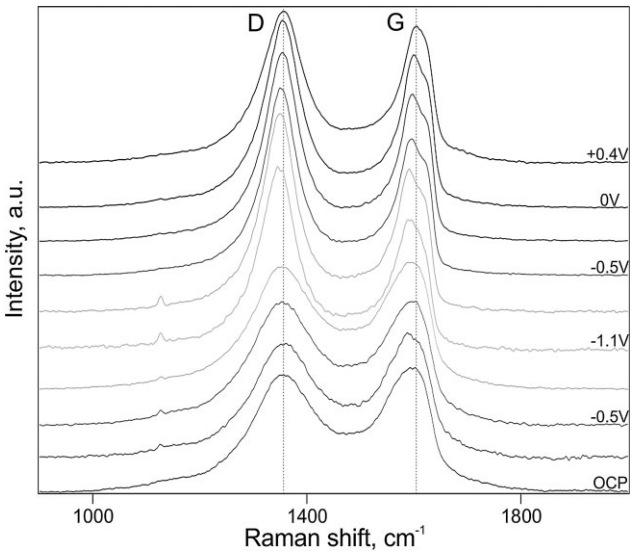

Figure 4 *In situ* Raman spectroelectrochemistry of FLGO during one electrochemical cycle, starting at the open circuit potential (OCP, 0.2 V vs. Ag/AgCl), with the potentials tagged on the right side of the spectra. The spectra are offset for clarity and normalized to the G band intensity (amplitude). Excitation wavelength is 514 nm.

K points in the Brillouin zone (BZ) of graphene, involving two zone-boundary phonons (TO-derived) for the 2D and one phonon and a defect for the D band [35, 36]. Both modes are dispersive spectral features, i.e., their frequencies vary linearly as a function of the energy of the incident laser, E_{laser}. The slope $\partial\omega_D/\partial E_{laser}$ is $\sim 50\,cm^{-1}\,eV^{-1}$, which is approximately one half of that of the 2D peak.

At first, the FLGO samples were checked by Raman spectroscopy *ex situ* before and after chronoamperometric cyclic (Fig. 3). As has been observed in the majority of works dealing with GO reduction, most of the treatment protocols induce an increased D/G ratio. It is, however, often misinterpreted as a sign of a progressive disruption of the remaining sp^2 network during reduction and thus lowering the lateral domain size L_a simply following the Tuinstra–Koenig relation $I_D/I_G = C(\lambda)/L_a$ [30], where $C(\lambda)$ is the excitation dependent proportionality constant. In contrast, this I_D/I_G increase has to be percepted in the frame of the amorphization trajectory introduced by Ferrari and Robertson [21], and recently corroborated by others [31, 32, 34]. In principle, the Tuinstra–Koenig relation fails when a certain defect density is reached and the aromatic rings are opening up, in the so-called stage 2 [21]. In this stage, the average distance between defects, L_D, is shown to be <3 nm in graphene and decreases further during amorphization [31]. Additionally, I_D/I_G is proportional to L_a^2 in this phase [21]. Increasing I_D/I_G in the reduced GO is thus reflecting the structural ordering in stage 2, i.e., the opposite of amorphization. Alongside with the relative G and D intensity change, both peaks are downshifted in the reduced FLGO. The D band redshift is caused by increasing the size of small aromatic clusters, which have higher modes [21]. The apparent redshift of the G + D′ peak is contradictory to [21] and its reason is unclear at the moment, but it may be rationalized by variations in relative G and D′ intensities together with narrowing. Such shape alterations may explain the inconsistencies regarding the G peak positions throughout the literature, with some of the works reporting G band downshift after reduction [2, 15, 37], while others showing the opposite [8] or no appreciable shift at all [18]. On the other hand, it is the peak narrowing, which confirms clearly the structural ordering upon reduction. Full-width-at-half-maxima of both G and D (denoted further as FWHM(G) and FWHM(D), respectively) decrease considerably during cycling. Further confirmation follows from the inset to Fig. 3, where the individual overtone and combination bands emerge from the hardly resolved bump.

The evolution of Raman spectra obtained *in situ* during electrochemical cycling of FLGO in 1M KOH is shown in Fig. 4 and the respective fitting parameters in Fig. 5, together with GNP treated under the same conditions. The potential range (−1.1 to +0.4 V versus Ag/AgCl) was chosen in order to avoid electrolysis of water accompanied by evolution of H_2 and O_2, which could damage the examined material.

Figure 5 demonstrates clearly the different impact of electrochemical cycling on the two tested materials, FLGO and GNP, similarly to Fig. 1. While the spectra of GNP undergo almost perfectly reversible changes in a very limited range of ± 2 and $\pm 3\,cm^{-1}$ for Pos(D) and Pos(G), respectively, ± 10 and $\pm 5\,cm^{-1}$ for FWHM(D) and FWHM(G), respectively, and ± 0.05 for I_D/I_G, the fluctuations in Raman spectra of FLGO are far more abrupt with a considerable hysteresis. The point of a sudden change, reflected in the band narrowing by ~ 50 and $25\,cm^{-1}$ for D and G bands, respectively, and I_D/I_G increase from 0.9 to 1.3, takes place at the most negative potential of the cycle. Interestingly, Pos(D) and I_D/I_G values return gradually close to the initial values, indicating a partial reversibility of the process. On the other hand, the linewidths keep the newly

© 2013 WILEY-VCH Verlag GmbH & Co. KGaA, Weinheim

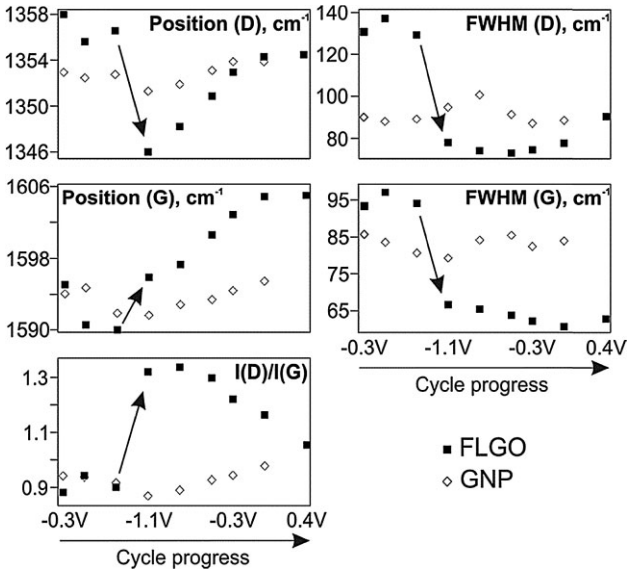

Figure 5 Evolution of selected fitting parameters of Raman G and D bands measured *in situ* during voltammetric cycling of FLGO (full rectangles) and GNP (empty diamonds) as a function of electrochemical potential (V vs. Ag/AgCl) in the cycle progression. The full sequence is: −0.3, −0.5, −0.8, −1.1, −0.8, −0.5, −0.3, 0.0, and +0.4V. Arrows inside the plots emphasize the sudden changes observed in FLGO Raman spectra. Excitation wavelength is 514 nm.

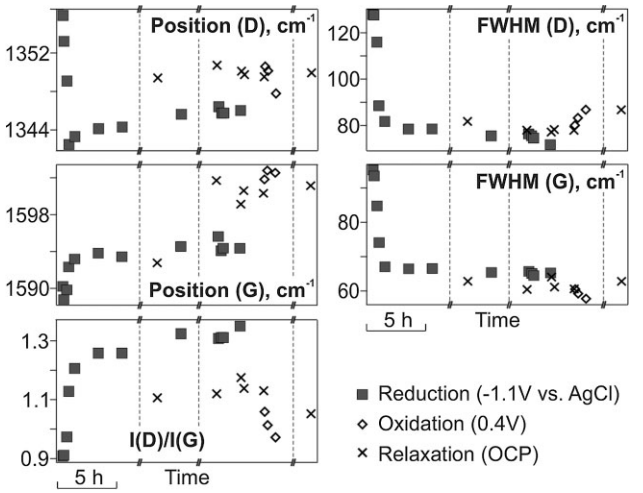

Figure 6 Evolution of selected fitting parameters of Raman G and D bands measured *in situ* during chronoamperometric charging of FLGO. The three individual vertical dashed lines indicate longer time breaks, during which the electrodes were left for relaxation: from left to right 1 day, 1 week, 1 day. Apart from the breaks, the timescale in the plots is indicated by the bar in the left bottom corners (5 h). Excitation wavelength is 514 nm.

acquired values with only small changes in the progressing cycle.

A more detailed account of the spectral changes during prolonged electrochemical treatment is given in Fig. 6. The initial stage of reduction at −1.1 V versus Ag/AgCl (∼0.9 V negative of OCP) lasting approx. 1 h inflicts the same changes to FLGO as discussed above, i.e., substantial G and D band narrowing, D band softening, G band stiffening and I_D/I_G ratio increasing.

However, ongoing reduction for additional 4 h at the same potential induces only small or even opposite effects. After 5 h of reduction, following values are reached and kept: Pos(D) at 1345 cm^{-1}, Pos(G) at 1594 cm^{-1}, FWHM(D) at 80 cm^{-1}, FWHM(G) at 67 cm^{-1}, and I_D/I_G at 1.25. The next 1-day relaxation at OCP causes visible stiffening of the peak frequencies and a lower I_D/I_G ratio, together with minor changes in the peak widths. Subsequent negative polarization, again at −1.1 V, results in peak shifts and I_D/I_G change close to the previous values at this potential. The small differences between the spectra at −1.1 V may be caused by structural reorganization during the relaxation linked to a slow desorption of gases (like CO_2) evolved during reduction. The next relaxation (1 week), followed immediately by negative polarization at −1.1 V (2 h) and another relaxation (2 h) cause almost exclusively sole "switching" between the two respective states with little hysteresis regardless the duration, even though a tiny progressive reduction can still be observed. However, a subsequent positive polarization at +0.3 V versus Ag/AgCl (∼0.6 positive of OCP) has a pronounced and gradual effect on the FLGO spectra. The changes are in part irreversible, as evidenced by the next 1-day relaxation. The irreversibility can be understood as physical oxidation associated with renewed creation of defects.

On the other hand, there might be several phenomena contributing to the reversible behavior of Raman features during this phase for both FLGO and GNP. The reversible peak softening at negative potentials and stiffening at positive potentials can be explained by changes in bond lengths upon charging [38], which causes lattice expansion/contraction in the presence of excess/lack of electrons. Such effects are well known from the studies of graphite intercalation compounds [39]. The more pronounced downshift during negative charging is probably due to a larger potential difference than during positive charging, when compared to OCP (−0.9 V vs. +0.6 V), hence the negative doping is larger. Another contribution to the observed variation of D and G band frequencies as well as of I(D)/I(G) ratio can come from a mild reversible reduction/oxidation. It should be emphasized that we do not observe (either in FLGO or GNP) the characteristic pattern of pristine graphene, where the G band stiffens under both electron and hole doping caused by the nonadiabatic removal of the Kohn anomaly from the Γ point [40].

4 Conclusions We have studied the behavior of few-layer graphene oxide and graphene nanoplatelets during electrochemical treatment by X-ray photoelectron spectroscopy and *in situ* Raman spectroscopy. The evolution of FLGO can be divided into two phases. During the first phase,

© 2013 WILEY-VCH Verlag GmbH & Co. KGaA, Weinheim

both under moderately fast cycling (voltammetric or chronoamperometric) and prolonged negative polarization, FLGO is reduced rapidly. The reduction, accompanied by structural ordering, is documented by lowering peaks belonging to oxygen-containing groups in XPS C1s and O1s spectra and by abrupt narrowing of Raman D and G linewidths. In this phase, the increase of the $I(D)/I(G)$ ratio evidences the structural ordering as well. The reduction degree can be compared to that achieved by a mild heating treatment in vacuum [8, 25]. This first phase in FLGO is irreversible and it is completely missing in the evolution of GNP. On the other hand, the second phase, both in FLGO and GNP, is dominated by only minor changes in the monitored parameters of Raman spectra. The G and D band shifts are governed by mild oxidation/reduction and/or by charging-induced lattice expansion during negative doping and lattice contraction during positive doping. In turn, the lattice expansion (contraction) is reflected in downshift (upshift) of the band frequencies. These variations are reversible. A small contribution of progressing reduction can still be traced in the FLGO in the second phase, again with no signs of such process in GNP.

Acknowledgements Financial support was provided by the Grant Agency of the Czech Republic (Contract No. 13-07724S) and FP7-Energy-2010-FET project Molesol (Contract No. 256617).

References

[1] S. Stankovich, D. A. Dikin, G. H. B. Dommett, K. M. Kohlhaas, E. J. Zimney, E. A. Stach, R. D. Piner, S. T. Nguyen, and R. S. Ruoff, Nature **442**, 282 (2006).
[2] S. Stankovich, D. A. Dikin, R. D. Piner, K. A. Kohlhaas, A. Kleinhammes, Y. Jia, Y. Wu, S. T. Nguyen, and R. S. Ruoff, Carbon **45**, 1558 (2007).
[3] X. Huang, X. Qi, F. Boey, and H. Zhang, Chem. Soc. Rev. **41**, 666 (2012).
[4] S. Mao, H. Pu, and J. Chen, RSC Adv. **2**, 2643 (2012).
[5] S. Pei and H.-M. Cheng, Carbon **50**, 3210 (2012).
[6] L. Kavan, J.-H. Yum, and M. Graetzel, ACS Appl. Mater. Interfaces **4**, 6999 (2012).
[7] W. S. Hummers and R. E. Offeman, J. Am. Chem. Soc. **80**, 1339 (1958).
[8] C. Mattevi, G. Eda, S. Agnoli, S. Miller, K. A. Mkhoyan, O. Celik, D. Mastrogiovanni, G. Granozzi, E. Garfunkel, and M. Chhowalla, Adv. Funct. Mater. **19**, 2577 (2009).
[9] H. Chen, M. B. Muller, K. J. Gilmore, G. G. Wallace, and D. Li, Adv. Mater. **20**, 3557 (2008).
[10] H. A. Becerril, J. Mao, Z. Liu, R. M. Stoltenberg, Z. Bao, and Y. Chen, ACS Nano **2**, 463 (2008).
[11] Y. Harima, S. Setodoi, I. Imae, K. Komaguchi, Y. Ooyama, J. Ohshita, H. Mizota, and J. Yano, Electrochim. Acta **56**, 5363 (2011).
[12] J. Kauppila, P. Kunnas, P. Damlin, A. Viinikanoja, and C. Kvarnström, Electrochim. Acta **89**, 84 (2013).
[13] W. Li, J. Liu, and C. Yan, Carbon **55**, 313 (2013).
[14] X.-Y. Peng, X.-X. Liu, D. Diamond, and K. T. Lau, Carbon **49**, 3488 (2011).
[15] G. K. Ramesha and S. Sampath, J. Phys. Chem. C **113**, 7985 (2009).
[16] Y. Shao, J. Wang, M. Engelhard, C. Wang, and Y. Lin, J. Mater. Chem. **20**, 743 (2010).
[17] H. Yu, J. He, L. Sun, S. Tanaka, and B. Fugetsu, Carbon **51**, 94 (2013).
[18] Z. Wang, X. Zhou, J. Zhang, F. Boey, and H. Zhang, J. Phys. Chem. C **113**, 14071 (2009).
[19] M. Zhou, Y. Wang, Y. Zhai, J. Zhai, W. Ren, F. Wang, and S. Dong, Chem. Eur. J. **15**, 6116 (2009).
[20] X. Du, I. Skachko, A. Barker, and E. Y. Andrei, Nature Nanotechnol. **3**, 491 (2008).
[21] A. C. Ferrari and J. Robertson, Phys. Rev. B **61**, 14095 (2000).
[22] H. Estrade-Szwarckopf, Carbon **42**, 1713 (2004).
[23] A. Siokou, F. Ravani, S. Karakalos, O. Frank, M. Kalbac, and C. Galiotis, Appl. Surf. Sci. **257**, 9785 (2011).
[24] D.-Q. Yang and E. Sacher, Langmuir **22**, 860 (2005).
[25] D. Yang, A. Velamakanni, G. Bozoklu, S. Park, M. Stoller, R. D. Piner, S. Stankovich, I. Jung, D. A. Field, C. A. Ventrice, and R. S. Ruoff, Carbon **47**, 145 (2009).
[26] A. C. Ferrari, J. C. Meyer, V. Scardaci, C. Casiraghi, M. Lazzeri, F. Mauri, S. Piscanec, D. Jiang, K. S. Novoselov, S. Roth, and A. K. Geim, Phys. Rev. Lett. **97**, 187401 (2006).
[27] A. Das, B. Chakraborty, S. Piscanec, S. Pisana, A. K. Sood, and A. C. Ferrari, Phys. Rev. B **79**, 155417 (2009).
[28] M. Kalbac, H. Farhat, J. Kong, P. Janda, L. Kavan, and M. S. Dresselhaus, Nano Lett. **11**, 1957 (2011).
[29] O. Frank, M. Bouša, I. Riaz, R. Jalil, K. S. Novoselov, G. Tsoukleri, J. Parthenios, L. Kavan, K. Papagelis, and C. Galiotis, Nano Lett. **12**, 687 (2012).
[30] F. Tuinstra and J. L. Koenig, J. Chem. Phys. **53**, 1126 (1970).
[31] L. G. Cançado, A. Jorio, E. H. M. Ferreira, F. Stavale, C. A. Achete, R. B. Capaz, M. V. O. Moutinho, A. Lombardo, T. S. Kulmala, and A. C. Ferrari, Nano Lett. **11**, 3190 (2011).
[32] A. Eckmann, A. Felten, A. Mishchenko, L. Britnell, R. Krupke, K. S. Novoselov, and C. Casiraghi, Nano Lett. **12**, 3925 (2012).
[33] M. Kalbac, O. Lehtinen, A. V. Krasheninnikov, and J. Keinonen, Adv. Mater. **25**, 1004 (2013).
[34] M. M. Lucchese, F. Stavale, E. H. M. Ferreira, C. Vilani, M. V. O. Moutinho, R. B. Capaz, C. A. Achete, and A. Jorio, Carbon **48**, 1592 (2010).
[35] P. Venezuela, M. Lazzeri, and F. Mauri, Phys. Rev. B **84**, 035433 (2011).
[36] J. Maultzsch, S. Reich, and C. Thomsen, Phys. Rev. B **70**, 155403 (2004).
[37] W. Chen, L. Yan, and P. R. Bangal, J. Phys. Chem. C **114**, 19885 (2010).
[38] L. Pietronero and S. Strässler, Phys. Rev. Lett. **47**, 593 (1981).
[39] M. S. Dresselhaus and G. Dresselhaus, Adv. Phys. **51**, 1 (2002).
[40] S. Pisana, M. Lazzeri, C. Casiraghi, K. S. Novoselov, A. K. Geim, A. C. Ferrari, and F. Mauri, Nature Mater. **6**, 198 (2007).

© 2013 WILEY-VCH Verlag GmbH & Co. KGaA, Weinheim

Short Communication Wiley Online Library ELECTROANALYSIS

DOI: 10.1002/elan.201300340

Progressive In Situ Reduction of Graphene Oxide Studied by Raman Spectroelectrochemistry: Implications for a Spontaneous Activation of $LiFePO_4$ (Olivine)

Milan Bousa,[a, b] Otakar Frank,*[a] and Ladislav Kavan[a, b]

Abstract: $LiFePO_4$ olivine (LFP) with few-layer graphene oxide (FLGO) was tested by repeated electrochemical charging/discharging. Here we report on a novel effect that the LFP/FLGO composite, which is electrochemically almost idle in a freshly made state, spontaneously enhances its activity, when the charge/discharge cycling progresses. Based on electrochemical, IR and Raman studies, we suggest that a gradual in situ reduction of FLGO is responsible for this activation.

Keywords: Graphene oxide · Electrochemical reduction · Lithium-ion battery · $LiFePO_4$ olivine

$LiFePO_4$ is a low-cost olivine-type material for the use in rechargeable lithium-ion batteries. It is highly stable during electrochemical cycling and environmentally friendly [1]. However, the poor electrical conductivity of LFP needs to be addressed either by doping or by carbon coating [2]. Various forms and amounts of carbonaceous materials were tested as coatings and conductive additives [1–10]. A simple mixing of LFP with carbon black resulted in a broad range of capacities from ca. 65 to 150 mAh/g [1,4,6]. Coating by a high surface area carbon at 600 °C represents another method to achieve capacities close to the nominal ones in a controllable manner [6]. The composite of LFP with multiwalled carbon nanotubes (MWCNT) exhibited similar performance, with a great difference between the activation ability of the carboxy-functionalized and non-functionalized MWCNTs, where the capacity reached 149 and 32 mAh/g, respectively [5]. Ding et al. [3] reported on the activation of LFP by reduced graphene oxide (RGO; reduced by hydrazine). However, long term sintering at 700 °C of the LFP/RGO composite was used and the electrode further contained 10 wt% of Super P carbon black. Similarly, Wang et al. [7] and Zhou et al. [8] activated LFP by graphene oxide (GO) which was subsequently treated by H_2/Ar at 600 °C, and the electrode further contained 15–20 wt% Super P carbon black. In all cases, charge capacities close to theoretical ones (~ 160 mAh/g) were found at the 0.1 C rate.

In all the examples cited above, the graphene has been used in a more or less oxidized form including RGO. Usually, graphite is used as a starting material, which is oxidized by the Hummer's method [11] followed by an exfoliation. The resulting graphene oxide usually consists of several graphene layers and contains oxidic functional groups, which make GO suspendable in polar solvents but decrease its conductivity due to the depletion in the conjugated sp^2 network [12]. Hence, in order to improve its charge-transfer properties, the GO needs to be partially reduced using a high temperature treatment and/or a reducing agent like hydrogen or hydrazine [3,7,8,13,14]. Electrochemical reduction has been successfully tested as well [15–20].

In this study we explored the electrochemical behavior of LFP in a composite with a non-calcined few layered graphene oxide (FLGO). To demonstrate the activation of LFP by FLGO, we avoided the presence of any other carbonaceous additives in our composites. The changes in the FLGO structure during electrochemical experiments were monitored separately by Raman and infrared spectroscopies.

Mixtures of LFP with 10% of oxidized MWCNT, FLGO (Cheap Tubes Inc., USA, 2–4 layers thick, overall C/O stoichiometry 2.75) and carbon black (CB) as reference materials were prepared by admixing the LFP powder into aqueous suspension (or isopropanol in the case of carbon black) of the respective additive, stirred overnight and evaporated to dryness. The homogeneity of dispersion of these materials was checked by scanning electron microscopy (SEM) (Figure 1). As can be seen from Figure 1B, oxidized MWNT perfectly entangle individual LFP crystallites. Similarly, thin FLGO veils and wraps the LFP particles (Figure 1C).

The as prepared mixtures were mixed with N-methyl-2-pyrrolidone (NMP) and polyvinylidene fluoride (PVDF)

[a] M. Bousa, O. Frank, L. Kavan
J. Heyrovský Institute of Physical Chemistry, v.v.i., Academy of Sciences of the Czech Republic, Dolejškova 3, CZ-18223 Prague 8, Czech Republic
*e-mail: otakar.frank@jh-inst.cas.cz

[b] M. Bousa, L. Kavan
Department of Inorganic Chemistry, Faculty of Science, Charles University, CZ-12840 Prague 2, Czech Republic

Supporting Information for this article is available on the WWW under http://dx.doi.org/10.1002/elan.201300340.

 © 2014 Wiley-VCH Verlag GmbH & Co. KGaA, Weinheim

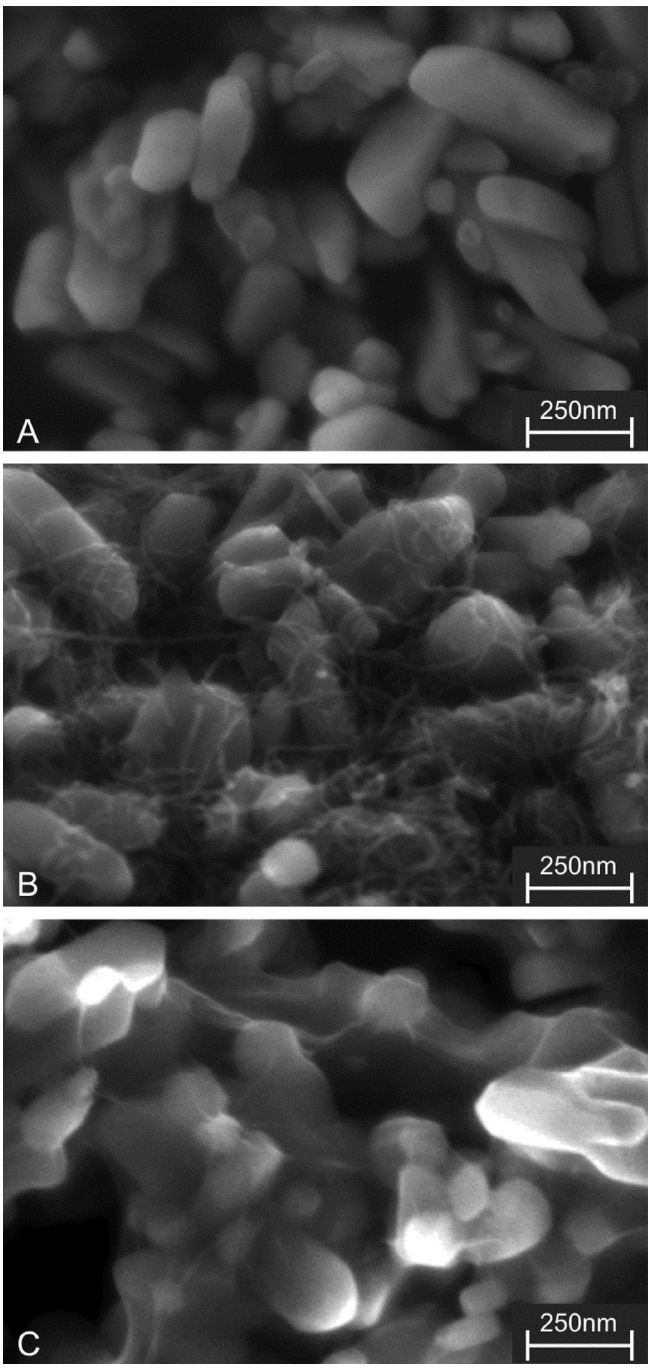

Fig. 1. SEM images of pristine LFP (A) and composites with 10% MWCNT (B) and 10% FLGO (C).

and doctor-bladed on conductive glass for the preparation of electrodes (see Experimental section in Supporting Information for details). The electrodes were subjected to galvanostatic, chronoamperometric or voltammetric cycling in 1 mol/L $LiPF_6$ in ethylene carbonate + dimethylcarbonate (EC/DMC; 1/1; w/w) with Li as reference and counter electrodes. Figure 2A shows charge capacities obtained from potential-step chronoamperometric cycling of a thick (~15 μm) LFP/FLGO electrode at the potential steps of 4.0 and 2.7 V vs. Li/Li^+ (the corresponding charge–discharge curves are depicted in Figure S2, Supporting Information). The composite exhibits considerable increase of charge capacities starting from ~0 mAh/g in the first cycles and reaching ~100 mAh/g after 105 cycles (ca. 70 hours). The process of charging and discharging is fully reversible (see Figure 2B), apart from the first ~10 cycles when the charge capacity is close to 0 and the detrermination of reversibility is less accurate. This peculiar activation effect was tested on two groups of electrodes with varying layer thickness of ~5 and ~15 μm, respectively. The inset in Figure 2A shows the dependence of the cycle number, when the electrode reaches its capacity maximum during chronoamperometric cycling (~ 85 ± 15 mAh/g) as a function of the thickness. As can be seen, thinner electrodes exhibit a much faster saturation, reaching the capacity of ~85 ± 15 mAh/g in the 10^{th}–15^{th} cycle. It should be noted that there is no correlation between the reached maximum capacity and the thickness of the electrodes. The lower capacity referenced to the nominal value of 160 mAh/g (Figure S1, Supporting Information) can be explained by the simple mechanical mixing followed by prolonged drying [21] or by the way of wrapping of LFP particles by FLGO, which was documented to have a large impact on the electrochemical performance of the resulting composite [10]. As shown in Figure S3 (Supporting Information), galvanostatic cycling has a similar activation effect on a fresh LFP/FLGO electrode as the chronoamperometric cycling.

Figure 2B shows a comparison of capacities from potentiostatic chronoamperometry for electrodes prepared by the same simple mixing of LFP with 10% of FLGO (the same electrode as in Figure 2A), MWNT and carbon black and in addition from LFP without an additive. While the pure LFP shows no appreciable capacities as expected, the LFP/CB electrode exhibits a capacity slightly over 20 mAh/g in the first cycle, followed by a constant drop finishing at values of 15 mAh/g in the 50^{th} cycle. The LFP/MWNT electrode shows more than 60 mAh/g in the first cycle, but again the capacity is decreasing continuously down to ~40 mAh/g in the 50^{th} cycle. The exceptional behaviour of LFP/FLGO points to a spontaneous activation of graphene oxide as a results of its progressive reduction by electrochemical cycling. The hypothesis is further corroborated by the faster activation of thinner electrodes, where the electrolyte can reach all the FLGO sheets much faster.

Figure 2C shows the results of galvanostatic cycling of an activated LFP/FLGO electrode at rates ranging from 10C to C/5 with cut-off voltages at 4.2 and 2.7 V (a different electrode than in Figure 2A). Coulombic efficiency is close to 100% except for the fastest C-rates, when the detrermination of reversibility is less accurate. The highest capacity at a rate of C/5 is 66 mAh/g, an example of charge–discharge curves at this C-rate is given in Figure S4 (Supporting Information). The electrode was activated by potential-step chronoamperometry as in the case of the electrode used in Figure 2A and its maximum chro-

 © 2014 Wiley-VCH Verlag GmbH & Co. KGaA, Weinheim

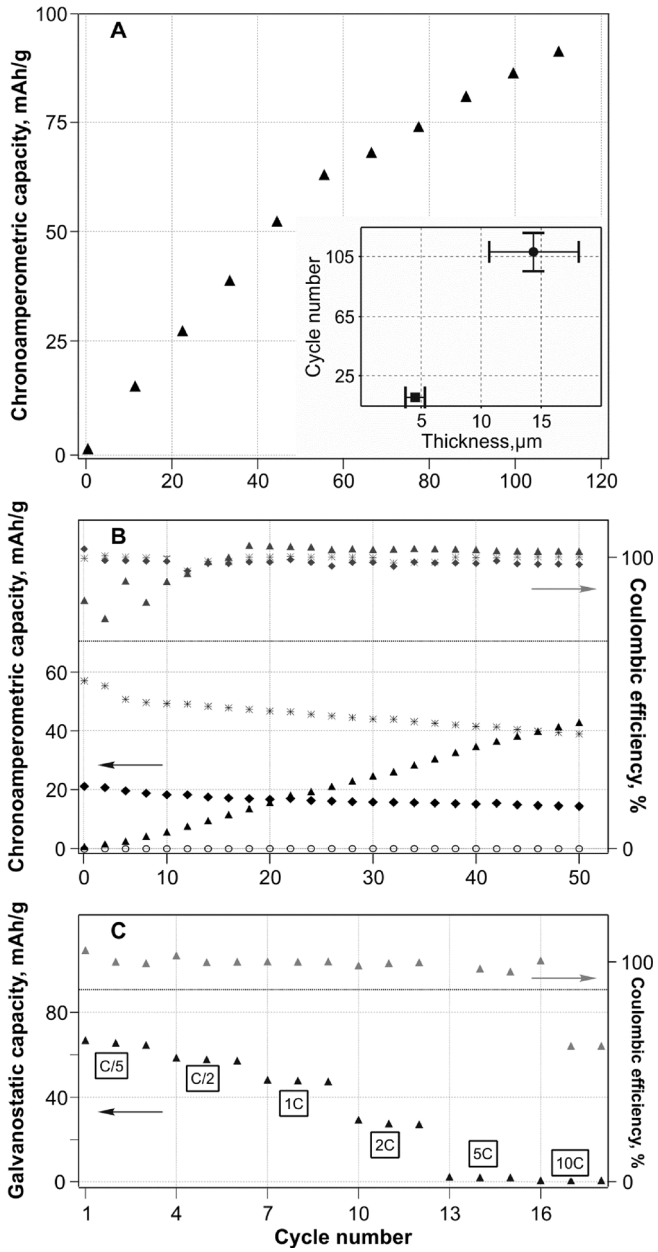

Fig. 2. (A) Chronoamperometric capacities of LFP/FLGO electrode. Data for every 10th cycle are plotted. Time of one complete cycle (charge and discharge) was 33 minutes. Inset: Dependence between electrode thickness and the cycle number, in which the capacity approaches its maximum for the particular electrode. (B) Capacities (left axis) obtained under the same conditions as in (A) of pristine LFP (circles) and its composites with MWCNT (stars), carbon black (diamonds) and FLGO (triangles), with the respective coulombic efficiencies on top (right axis). (C) Galvanostatic discharge capacity of LEP/FLGO (left axis) at varying C-rates and the respective coulombic efficiencies (right axis).

noamperometric capacity was ~70 mAh/g at 3600 s step duration.

Figure 3 shows the evolution of cyclic voltammograms of the LFP/FLGO sample during progressive cycling at a scan rate of 1 mV/s. Similarly to chronoamperometric and galvanostatic cycling, the peak current densities in the first cycle reach only 1 μA/cm^2, after which they steadily increase e.g. in the 13th cycle to reach almost 230 μA/cm^2. During the voltammetric cycling the separation of the cathodic and anodic peaks increases, but stabilizes at around 20th scan. The peak-to-peak separation at a scan rate of 0.1 mV/s in a stabilized LFP/FLGO electrode was 0.169 V (Inset A in Figure 3) which compares favorably to the value of 0.191 V reported by Wang et al.[7] The voltammetric charge and discharge capacities increase accordingly up to 40 mAh/g (the difference to the chronoamperometric cycling is caused by different experimental conditions especially the cycle duration), and show an almost ideal reversibility (Inset B in Figure 3).

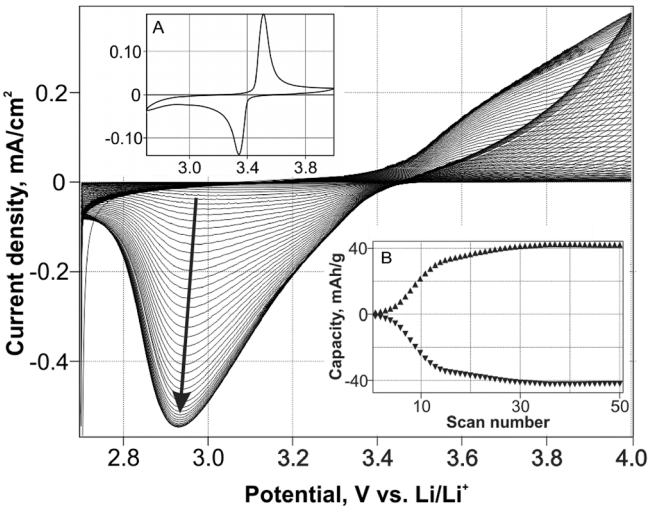

Fig. 3. Cyclic voltammograms (50 scans) of LFP/FLGO electrode at a scan rate of 1 mV/s. The increase of current densities through ongoing cycling is indicated by an arrow. Inset A: Cyclic voltammogram at a scan rate of 0.1 mV/s. Inset B: Progressive evolution of capacities calculated from the cyclic voltammetry cycling.

Raman spectroscopy can provide a useful insight into the changes of the FLGO structure, which occur during the electrochemical experiments. Ex situ Raman spectra of pristine FLGO and LFP/FLGO electrode before and after chronoamperometric cycling are shown in Figure 4. Apart from a low-intensity band at ~950 cm^{-1} in the spectra of LFP/FLGO, which belongs to the PO_4 stretching vibration [22], two main features are observed in the spectra of both samples. The first one centered at ca. 1320 cm^{-1} belongs to the intravalley double resonance D mode, which requires a defect in the sp^2 carbon network for its activation, while the second one at ca. 1600 cm^{-1} is a convolution of the single resonance tangential E_{2g} "graphitic" G mode (~1580 cm^{-1}) and the intervalley defect-induced double resonance D′ mode (~1610 cm^{-1}) [23,24]. Obviously, there is a distinct evolution of the FLGO during electrochemical cycling. The main parameters of the D and G bands are plotted in Figure 4B–E as a function of cycle number, with the D band fitted with

 © 2014 Wiley-VCH Verlag GmbH & Co. KGaA, Weinheim

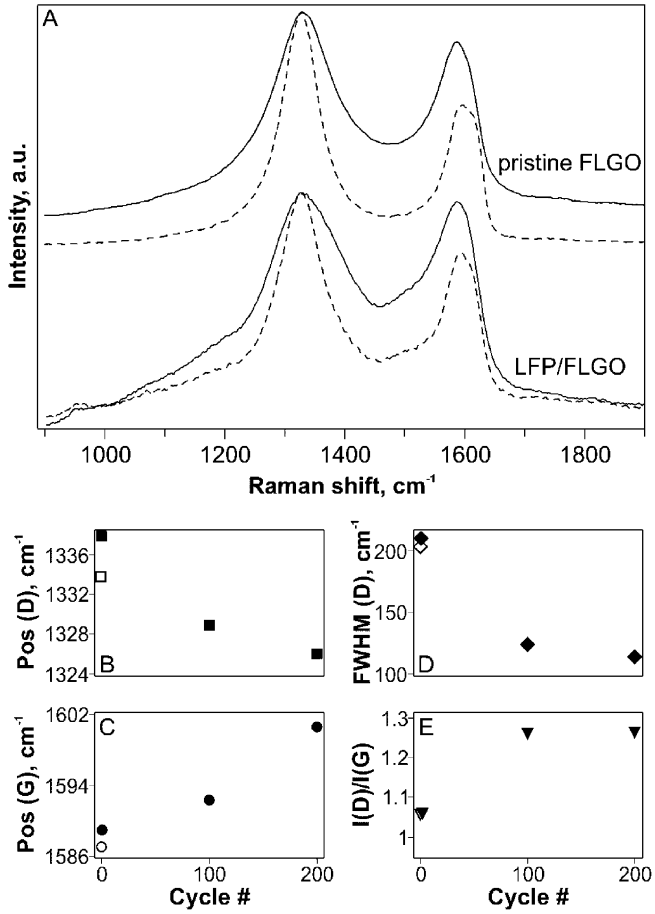

Fig. 4. Raman spectra of pristine FLGO and LFP/FLGO composite electrodes before (solid line) and after (dashed line) 100 chronoamperometric cycles. Bottom plots show the evolution of D and G band frequencies, D linewidths and I(D)/I(G) intensity ratio during the electrochemical cycling. Data are obtained by ex situ Raman spectroscopy of unused fresh-made (empty symbols) and wetted (full symbols) electrodes before measuring and after 100 and 200 cycles, respectively. Excitation wavelength was 633 nm.

a Lorentzian shape and the G+D′ bands are treated as one asymmetric band approximated with Breit-Wigner-Fano lineshape, as suggested for highly disordered carbons [23]. The D band frequency decreases as well as its linewidth, while the G band frequency increases. The D/G intensity ratio (I(D)/I(G); measured as amplitudes) increases. The D band downshift is caused by increasing the size of small aromatic clusters, which have higher vibrational modes [23]. In the same time, the D band narrowing confirms clearly the structural ordering upon cycling. The simultaneous G band upshift and increase of I(D)/I(G) can be rationalized in the frame of amorphization diagram introduced by Ferrari and Robertson [23]. Taking into account the structural ordering and increase of aromatic cluster size evidenced by the D band evolution, the G band evolution (both the frequency and intensity) corresponds to the amorphization stage 2, but on the "ordering" trajectory [23,25]. It is evident that a careful analysis of many parameters of the Raman bands ensures a proper interpretation of the results. This concerns especially the I(D)/I(G) ratio, which alone is often considered as a straightforward indicator of disorder in sp^2 systems, or even directly used for quantification of the lateral crystallite size L_a according to the Tuinstra-Koenig relation [24]. However, this equation is valid only for the amorphization stage 1 [23,25,26]. In principle, the Tuinstra–Koenig relation fails when a certain defect density is reached and the aromatic rings are opening up, in the so-called stage 2 [23]. In this stage, the average distance between defects, L_D, is shown to be less than 3 nm in graphene and decreases further during amorphization [25]. Additionally, I(D)/I(G) is proportional to L_a^2 in this phase [23]. Increasing I(D)/I(G) and *Pos*(G) in the reduced FLGO is thus reflecting the structural ordering in stage 2, i.e. the opposite of amorphization.

The progressive reduction of FLGO upon electrochemical cycling is further evidenced by Fourier transform infrared spectroscopy (Figure S5, Supporting Information). Some of the peaks initially present in the FLGO lose their intensities or completely vanish during the cycling, namely 1120 cm^{-1}, 1305 cm^{-1} and 1505 cm^{-1}, which can be tentatively assigned to oxygen-containing functional groups (ester C–O–C, or C–O in carboxylic groups). Two peaks in the aromatic-rings-vibrations region (1630 and 1765 cm^{-1}) markedly shift, indicating pronounced changes of the graphitic structure.

The reduction of FLGO induced by electrochemical cycling, but in aqueous electrolyte solutions, was evidenced also by in situ Raman spectroelectrochemistry and ex situ X-ray photoelectron spectroscopy, which confirmed the structural rearrangement and loss of oxygen-containing functional groups [27].

In summary, we have reported on a simple way of a spontaneous electrochemical activation of a few-layer graphene oxide performing as a conductive additive to a nanocrystalline $LiFePO_4$ olivine. In contrast to previous studies [3,7,8], where the graphene oxide was reduced during the electrode preparation process at a temperature of at least 600 °C, we show that a charge/discharge cycling of the nanocomposite results in a progressive reduction of the FLGO, which in turns leads to a gradual capacity increase of the tested material of up to 100±15 mAh/g.

Acknowledgements

This work was supported by the *Grant Agency of the Czech Republic* (Contract No. 13-07724S). We are thankful to *I. Jirka* for chemical characterization of FLGO.

References

[1] A. K. Padhi, K. S. Nanjundaswamy, J. B. Goodenough, *J. Electrochem. Soc.* **1997**, *144*, 1188.
[2] W.-J. Zhang, *J. Power Sources* **2011**, *196*, 2962.
[3] Y. Ding, Y. Jiang, F. Xu, J. Yin, H. Ren, Q. Zhuo, Z. Long, P. Zhang, *Electrochem. Commun.* **2010**, *12*, 10.

 © 2014 Wiley-VCH Verlag GmbH & Co. KGaA, Weinheim

[4] K. Dokko, K. Shiraishi, K. Kanamuraa, *J. Electrochem. Soc.* **2005**, *152*, A2199.
[5] L. Kavan, R. Bacsa, M. Tunckol, P. Serp, S. M. Zakeeruddin, F. Le Formal, M. Zukalova, M. Graetzel, *J. Power Sources* **2010**, *195*, 5360.
[6] C.-Z. Lu, G. T.-K. Fey, H.-M. Kao, *J. Power Sources* **2009**, *189*, 155.
[7] L. Wang, H. Wang, Z. Liu, C. Xiao, S. Dong, P. Han, Z. Zhang, X. Zhang, C. Bi, G. Cui, *Solid State Ionics* **2010**, *181*, 1685.
[8] X. Zhou, F. Wang, Y. Zhu, Z. Liu, *J. Mater. Chem.* **2011**, *21*, 3353.
[9] B. Wang, D. Wang, Q. Wang, T. Liu, C. Guo, X. Zhao, *J. Mater. Chem. A* **2013**, *1*, 135.
[10] W. Wei, W. Lv, M.-B. Wu, F.-Y. Su, Y.-B. He, B. Li, F. Kang, Q.-H. Yang, *Carbon* **2013**, *57*, 530.
[11] W. S. Hummers, R. E. Offeman, *J. Am. Chem. Soc.* **1958**, *80*, 1339.
[12] D. A. Dikin, S. Stankovich, E. J. Zimney, R. D. Piner, G. H. B. Dommett, G. Evmenenko, S. T. Nguyen, R. S. Ruoff, *Nature* **2007**, *448*, 457.
[13] S. Stankovich, D. A. Dikin, R. D. Piner, K. A. Kohlhaas, A. Kleinhammes, Y. Jia, Y. Wu, S. T. Nguyen, R. S. Ruoff, *Carbon* **2007**, *45*, 1558.
[14] L. Kavan, J.-H. Yum, M. Graetzel, *ACS Appl. Mater. Interf.* **2012**, *4*, 6999.
[15] G. K. Ramesha, S. Sampath, *J. Phys. Chem. C* **2009**, *113*, 7985.
[16] Y. Harima, S. Setodoi, I. Imae, K. Komaguchi, Y. Ooyama, J. Ohshita, H. Mizota, J. Yano, *Electrochim. Acta* **2011**, *56*, 5363.
[17] X.-Y. Peng, X.-X. Liu, D. Diamond, K. T. Lau, *Carbon* **2011**, *49*, 3488.
[18] J. Kauppila, P. Kunnas, P. Damlin, A. Viinikanoja, C. Kvarnström, *Electrochim. Acta* **2013**, *89*, 84.
[19] W. Li, J. Liu, C. Yan, *Carbon* **2013**, *55*, 313.
[20] H. Yu, J. He, L. Sun, S. Tanaka, B. Fugetsu, *Carbon* **2013**, *51*, 94.
[21] L. Chen, M. Zhang, W. Wei, *J. Nanomater.* **2013**, *2013*, 940389.
[22] M. T. Paques-Ledent, P. Tarte, *Spectrochim. Acta A* **1974**, *30*, 673.
[23] A. C. Ferrari, J. Robertson, *Phys. Rev. B* **2000**, *61*, 14095.
[24] F. Tuinstra, J. L. Koenig, *J. Chem. Phys.* **1970**, *53*, 1126.
[25] L. G. Cançado, A. Jorio, E. H. M. Ferreira, F. Stavale, C. A. Achete, R. B. Capaz, M. V. O. Moutinho, A. Lombardo, T. S. Kulmala, A. C. Ferrari, *Nano Lett.* **2011**, *11*, 3190.
[26] M. M. Lucchese, F. Stavale, E. H. M. Ferreira, C. Vilani, M. V. O. Moutinho, R. B. Capaz, C. A. Achete, A. Jorio, *Carbon* **2010**, *48*, 1592.
[27] M. Bousa, O. Frank, I. Jirka, L. Kavan, *Phys. Status Solidi B*, **2013**, DOI: 10.1002/pssb.201300105, in press..

Received: July 17, 2013
Accepted: September 9, 2013
Published online: October 11, 2013

 © 2014 Wiley-VCH Verlag GmbH & Co. KGaA, Weinheim

NANO LETTERS

Letter

pubs.acs.org/NanoLett

Phonon and Structural Changes in Deformed Bernal Stacked Bilayer Graphene

Otakar Frank,*[,†,‡] Milan Bouša,[†,§] Ibtsam Riaz,[∥] Rashid Jalil,[∥] Kostya S. Novoselov,[∥] Georgia Tsoukleri,[‡,⊥] John Parthenios,[‡] Ladislav Kavan,[†] Konstantinos Papagelis,*[,‡,#] and Costas Galiotis[‡,#]

[†]J. Heyrovsky Institute of Physical Chemistry of the AS CR, v.v.i., Prague 8, Czech Republic

[‡]Institute of Chemical Engineering and High Temperature Chemical Processes, Foundation of Research and Technology-Hellas (FORTH/ICE-HT), Patras, Greece

[§]Department of Inorganic Chemistry, Faculty of Science, Charles University, Prague 2, Czech Republic

[∥]School of Physics and Astronomy, University of Manchester, Manchester, U.K.

[⊥]Interdepartmental Programme in Polymer Science and Technology, University of Patras, Patras, Greece

[#]Materials Science Department, University of Patras, Patras, Greece

Supporting Information

ABSTRACT: We present the first Raman spectroscopic study of Bernal bilayer graphene flakes under uniaxial tension. Apart from a purely mechanical behavior in flake regions where both layers are strained evenly, certain effects stem from inhomogeneous stress distribution across the layers. These phenomena such as the removal of inversion symmetry in bilayer graphene may have important implications in the band gap engineering, providing an alternative route to induce the formation of a band gap.

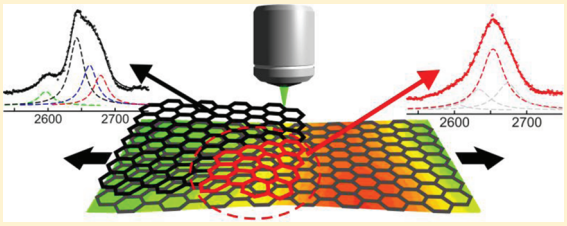

KEYWORDS: *Bilayer graphene, Raman spectroscopy, strain, tension, band gap*

Graphene, one atom thick membrane,[1] is the thinnest known elastic material, exhibiting exceptional electronic and mechanical properties.[2] Many applications directly exploiting its Young's modulus of ca. 1 TPa and strength over 160 GPa[3] are envisaged or even already tested, such as mechanical resonators,[4] strain sensors,[5,6] or graphene-based composites.[7] Bilayer or multilayer graphenes, owing to their distinct electronic band structures, have extraordinary potential for next-generation optoelectronics and post-silicon nanoelectronics.[8−10]

According to recent calculations, a band gap opening in monolayer graphene by the sole application of a uniaxial strain is hardly feasible.[11−13] The situation could be more promising when a combination of uniaxial and shear strains would be applied; however, the theory predicts large strains between 12 and 17% to open a band gap.[14] Recently, significant effort has been put into bilayer graphene, which seems to be more promising in terms of opening a sizable band gap. Inequality between the two layers caused by different carrier concentrations has already proven successful in opening a measurable band gap[8,15,16] due to a local symmetry breaking.[17] Even though external electric fields have been employed to control the energy gaps in several forms of graphene,[8,10,15,16] a simple and practical method of tuning the electronic energy gaps based on pure mechanical deformations is still lacking. For this purpose, since uniaxial stress is not supposed to open up a band gap at reasonably low strain levels,[18,19] it is worth considering the inducement of an inhomogeneous strain as a viable tool.[20,21]

At the moment, there is no detailed experimental study on strained bilayer graphene. Hence, it is of utmost importance to understand its response upon mechanical loading. Basic experimental data sets already exist for monolayer graphene,[3,5,22−29] and thus a direct comparison is available to assess the influence of the second layer and the electronic interaction provided by its presence.

With this respect, Raman spectroscopy is the key diagnostic tool to monitor the number of layers and their changes under external force.[30−32] The G band is a first-order Raman mode and corresponds to the in-plane, zone center, doubly degenerate phonon mode with E_{2g} symmetry.[33] The D and 2D modes come from a second-order double resonant process between nonequivalent K points in the Brillouin zone (BZ) of graphene, involving two zone−boundary phonons for the 2D and one phonon and a defect for the D band.[34]

In general, tensile strain induces phonon softening (red-shift) and compression causes phonon hardening (blue shift). In addition, the G peak splits into two components due to symmetry lowering of the crystal lattice in both cases.[24,26,35] The subpeaks denoted G^- and G^+ shift at rates ∼30−33 and

Received: October 10, 2011
Revised: November 27, 2011
Published: December 13, 2011

ACS Publications © 2011 American Chemical Society

dx.doi.org/10.1021/nl203565p | *Nano Lett.* 2012, 12, 687−693

~10−14 cm^{-1}/%, respectively, both under uniaxial tension[24,26,29] and low levels of compression.[24] These shift rates agree well with recent calculations.[13,26] Additionally, the splitting of the 2D peak has been reported for some graphene samples as well.[23,29,36] As it turns out, the origin of this behavior is quite complex, and the observed effects strongly depend on the excitation wavelength and the mutual orientation of the graphene lattice, strain direction, and incident/scattered light polarization.[23,29,36−38] Although the splitting and/or asymmetrical broadening indeed influence the observed behavior, the 2D peak strain-shift rate has been found by various authors between 45 and 65 cm^{-1}/%.[23,24,26,28,29] A biaxial strain induces shift of the Raman peaks at rates approximately double those observed in uniaxial tension.[27,39,40]

In this work, we have undertaken a detailed Raman study of several samples of bilayer graphene embedded in polymer matrix and compared their behavior under uniaxial tension with that of monolayer parts of the same flakes. A careful examination along and across the whole flake area was conducted in order to identify the presence of inhomogeneities in the induced strain field due to an uneven stress transfer or slippage either along the polymer/graphene interface or between the two graphene layers. Three excitation wavelengths were used to provide a more coherent picture, especially for the 2D band. Raman features, seen for the first time in mechanically deformed graphene bilayer, are discussed with regards to changes in the local symmetry and possible band gap opening.

Graphene flakes containing both a mono- and bilayer part were subjected to tensile strain by means of a cantilever beam assembly,[24,28] and their G and 2D bands were monitored by Raman spectroscopy using 785 nm (1.58 eV), 633 nm (1.96 eV), and 514.5 nm (2.41 eV) excitation. The flakes were either laid bare on a polymer substrate or covered by another polymer layer to minimize a possible slippage during loading.

Figure 1a shows the evolution of the Raman G bands in the embedded mono- and bilayer graphene (flake F1) under tension using the 785 nm laser excitation. As can be seen, both the bi- and monolayer show the same behavior; i.e., their G bands red-shift and split into two components due to the removal of degeneracy of the E_{2g} phonon.[24,26,35] In Figure 1b, both the mono- and bilayer exhibit the same shift rates of −31.3 and −9.9 cm^{-1}/% for G^- and G^+, respectively, in accordance with previous experimental results[24,26,29] as well as theoretical predictions.[13,26] The configuration of the respective layers can be seen on a micrograph in Figure 1c. As can be deduced from the image, as well as from the G^-/G^+ relative intensities of the respective layers, they belong to the same flake, part of which is composed of a single layer, whereas the other part is overlaid by another layer with Bernal (AB) stacking. Therefore, the lattice orientation, which can be calculated from the G^-/G^+ relative intensities,[23,26,29,35] is the same for the mono- and bilayer, namely ~21° (with respect to the zigzag direction and strain axis). The indicated polarization dependence of the measured spectra, which shows exactly opposite G^-, G^+ intensities when the incident light polarization is rotated by 90°, clearly confirms the above. The linearity of the sub-band evolution (Figure 1b) as well as their shift rates indicate an efficient stress transfer from the embedding polymer to the measured graphene. This issue has been recently found to be of a great importance for a proper analysis of the experimental data.[28,41,42] To avoid misinterpretation, we scanned the laser beam over the whole

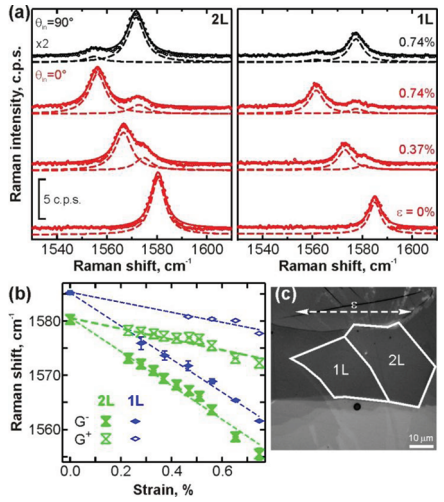

Figure 1. (a) G band Raman spectra of strained monolayer (right) and bilayer (left) graphene flake F1 excited by 785 nm. Dashed curves are Lorentzian fits of the individual components with solid lines as their convolution, and the points represent experimental spectra. Plot (b) shows the evolution of the position of the G^- and G^+ sub-bands with strain. Dashed lines represent linear fits to the experimental data. Error bars are one standard deviation to all data measured at the given point and strain level. Panel (c) shows an optical micrograph of the flake F1. The strain axis, ε, is depicted with a horizontal arrow.

flake area at selected stages of the tensile loading and checked the consistency of the Raman shifts.

The 2D band evolution with strain for the monolayer (panels a−c) and bilayer (panels d−f) parts of the flake F1 are shown in Figure 2. In agreement with recent observations,[23,29,36] there is a clear splitting in the monolayer 2D peak (Figure 2a). Under parallel laser polarization, this spectral feature (Figure 2a, red spectra) can be approximated using two Lorentzian lines with shift rates of −41.5 and −22.4 cm^{-1}/% for the lower (purple) and higher (red) frequency component, respectively, as obtained using a linear fit (Figure 2b). The faster-shifting (lower frequency) component becomes much more intense with increasing strain under parallel polarization (Figure 2c), in contrast to the perpendicular polarization, where the two components are of a similar intensity throughout the whole experiment (for more details, see ref 23). There seems to be a broad consensus that this splitting is caused by unequivalent K−K′ pairs in the deformed Brillouin zone and a differing contribution of the so-called inner or outer processes.[23,29,36−38] Furthermore, the amount of splitting depends on the orientation of the sample, laser polarization, and excitation wavelength.[23,38] The Raman 2D mode in bilayer graphene (Figure 2d−f) is expected to be affected by the strain-induced electronic changes since it arises from a double resonance process that involves transitions among various electronic states.[31,32,43] Consequently, the larger fwhm of the 2D peak in bilayer graphene compared to that of the monolayer makes the assignment of the deconvoluted peaks a rather difficult task. More specifically, in bilayer graphene having Bernal configuration the dispersion of π-electrons and phonon bands near the K point of the Brillouin zone split both into two components with specific symmetries (Figure 2g). The electronic branches split into two conduction (π_1^*, π_2^*) and two valence (π_1, π_2) bands, while the dispersion is parabolic near the K point (Figure 2g). The π_1 and π_1^* bands are degenerate at K, and the π_2 and π_2^* ones exhibit an energy gap

dx.doi.org/10.1021/nl203565p | Nano Lett. 2012, 12, 687−693

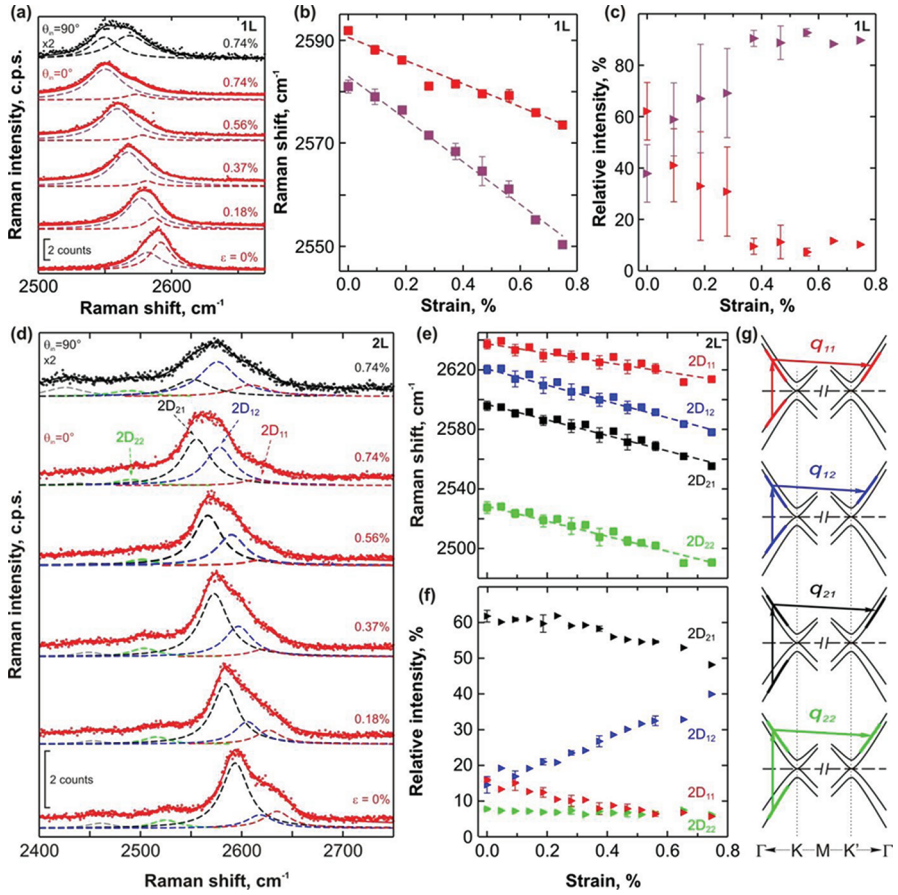

Figure 2. 2D band Raman spectra of strained (a) mono- and (d) bilayer graphene flake F1 excited by 785 nm. Dashed curves are Lorentzian fits of the individual components with solid lines as their convolution, and the points represent experimental spectra. Plots (b) and (e) show the evolution of the position of the individual Lorentzian components with strain in the mono- and bilayer, respectively, while plots (c) and (f) show the evolution of the relative intensities of the respective components (all with $\theta_{in} = 0°$). Error bars are one standard deviation to all data measured at the given point and strain level. (g) Schematic sketches depicting the four processes in bilayer graphene; for a better clarity, only the first scattering q_{ij} events are plotted.

of about 0.8 eV.[32,43,44] Group theory for bilayer graphene predicts four dinstict DR processes along the Γ−K−M−K′−Γ direction.[32] It should be noted that along the aforementioned BZ direction the electron−phonon coupling between the iTO (in-plane transverse optical) phonons and π-electrons near K and K′ has the highest oscillation strength.[43] The four processes can be assigned as D_{ij} where i (j) denotes an electron scattered from (to) each conduction band $\pi_{i(j)}$*. The lower (π_1*) and upper (π_2*) conduction bands belong to different irreducible representations (T_1 and T_2, respectively). Also, the iTO phonon branch splits into two branches related to the symmetric (assigned as S and correspond to T_1 irreducible representation) and antisymmetric (assigned as AS and correspond to T_2 irreducible representation) phonons, with respect to the inversion symmetry. According to electron−phonon selection rules, the S phonons are connected with the D_{11} and D_{22} processes involving electrons with the same symmetry, whereas the AS phonons occur for processes D_{12} and D_{21} involving electrons with different symmetries. Since the iTO phonon frequency increases with increasing q (due to the Kohn anomaly at K point[32]), the highest (lowest) frequency peak of the 2D band is associated with D_{11} (D_{22}) process. Experimentally, the 2D band line shape of a Bernal-stacked bilayer graphene is fitted by four Lorentzian components, each having the same fwhm of ∼24 cm^{-1} (Figure 4d, bottom spectrum).[31,32]

Under tension, the shape of the bilayer 2D band clearly changes (Figure 2d). The evolution of the four sub-bands can be monitored credibly only when the fitting is carried out using components of equal widths at a given strain level. Also, in a very recent high-pressure doping Raman study of bilayer graphene, Nicolle et al. followed a similar fitting protocol.[45] As can be seen in Figure 2e, the positions of the components follow linear trends with similar rates of ∼−50 cm^{-1}/% for the three lower frequency components ($2D_{22}$, $2D_{21}$, and $2D_{12}$) and a smaller shift rate of −29 cm^{-1}/% for the highest frequency component $2D_{11}$. The intensities of the components are changing unevenly, too (Figure 2f); the intensity of the $2D_{12}$ component increases, mainly at the cost of the neighboring $2D_{21}$ and $2D_{11}$ with the latter almost diminishing at higher strains.

It is interesting to compare the two sub-bands of the monolayer 2D peak (Figure 2a−c) and the two highest frequency components $2D_{11}$ and $2D_{12}$ in the bilayer (Figure 2d−f). As mentioned above, the $2D_{11}$ component originates from the processes associated with the "original" π_1 and π_1* bands degenerated at the K point, while the other three lower wavenumber components involve at least one electron or hole from the π_2 and π_2* bands.[31,32,43,44] Bearing that in mind, a

dx.doi.org/10.1021/nl203565p | Nano Lett. 2012, 12, 687−693

plausible scenario might be suggested to explain the observed shift rates and the evolution of intensities. Let us consider a splitting of the $2D_{11}$ component in the same way as in the monolayer 2D band. Then, what we observe as the $2D_{11}$ component in the strained bilayer—with smaller shift rate and decreasing intensity—would be actually only the higher wavenumber subcomponent (compare red symbols in Figure 2e,f and in Figure 2b,c), whereas the lower wavenumber subcomponent would gradually shift toward the $2D_{12}$ component and merge with it (blue symbols in Figures 2e,f vs purple symbols in Figure 2b,c), causing its apparent intensity to increase upon stretching. The change of the bilayer 2D band shape recorded under perpendicular laser polarization might be connected with the observed concomitant alterations in the monolayer (black curves in Figure 2a,d). The discussed $2D_{11}$ splitting can further supported by the work of Mafra et al.,[46] who pointed out the importance of the inner scattering processes in Bernal bilayer graphene. Hence the complex line shape of the 2D Raman signal comes from the contribution of the inner and outer processes due to the anisotropy of both the electron and phonon dispersions.[46] Our experimental data show that the $2D_{11}$ component is more sensitive to modifications in the electronic and/or phononic structure, while the degree of splitting is not that pronounced for the other components. However, more theoretical work about the double resonance mechanisms in graphene systems is necessary to understand fully the effect of strain upon the changes in the line shape of the 2D peak.

As mentioned above, the monolayer 2D peak splitting depends strongly on the excitation wavelength. Therefore, we have examined another flake (F2) composed of mono- and bilayer graphene using a different excitation line of 633 nm (Figure 3). At a certain strain level, which is apparently higher in the monolayer than in the bilayer, a failure in the stress uptake can be seen (labeled with a dotted vertical line in Figure 3b,d). Up to the failure, the monolayer 2D peak exhibits no obvious splitting (shift rate of −48.5 cm^{-1}/%), but only a slight asymmetry and broadening in the final stages of the experiment. An important issue arises here; Huang et al.[36] and Yoon et al.[29] using the 532 nm (2.33 eV) and 514.5 nm (2.41 eV) excitations, respectively, reported a clear 2D splitting for strain applied essentially along the armchair and zigzag directions. Our measurements[28] using the 514.5 nm excitation showed a relatively small 2D peak broadening at a rate of 11 cm^{-1}/% and, apparently, absence of splitting. On the contrary, using the 785 nm (1.58 eV) excitation, a significant nonlinear fwhm enhancement is observed, reaching ∼43 cm^{-1} at strain of only 0.7% for ∼20° lattice orientation.[23] Furthermore, the data presented here using an 633 nm (1.96 eV) excitation showed a shift rate of 17 cm^{-1}/% for the fwhm of the 2D (15° lattice orientation), indicating a progressive fwhm increase when the excitation energy is red-shifted. This experimental evidence is in contrast with recent calculations of Venezuela et al.,[38] who predicted the opposite trend, namely that the 2D line becomes broader in an asymmetric double peak structure, at higher excitation energies up to ultraviolet range. Therefore, our observations confirm that Raman data using various excitation wavelengths and sample orientations are extremely important to fully resolve the double resonance process in graphene systems.

In contrast to the flake F1 (Figure 2d–f; λ_{exc} = 785 nm), all four Lorentzian components of the bilayer 2D band in flake F2 (Figure 3c–e; λ_{exc} = 633 nm) exhibit almost identical shift rates

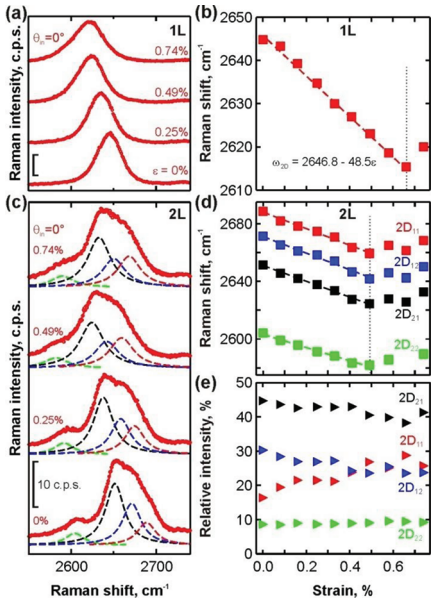

Figure 3. 2D band Raman spectra of strained (a) mono- and (c) bilayer graphene flake F2 excited by 633 nm. Dashed curves are Lorentzian fits of the individual components with solid lines as their convolution and the points represent experimental spectra. Plots (b) and (d) show the evolution of the position of the individual Lorentzian components with strain in the mono- and bilayer, respectively; plot (e) shows the evolution of the relative intensities of the respective components for the bilayer part. In panels (b) and (d), dotted lines mark the failure strain level, and dashed lines represent linear fits to the experimental data up to the failure.

of ∼−55 cm^{-1}/% and only minor changes in relative intensities. Here, the absence of splitting in the monolayer seems to be reflected in the uniform evolution of the bilayer 2D band components. This justifies our previous statement on the higher sensitivity of the $2D_{11}$ component, which apparently correlates with the 2D band behavior of the neighboring monolayer.

In Figure 4a, a detailed Raman mapping of flake F2 strained to 0.74% (Figure 4a; λ_{exc} = 633 nm) reveals inhomogeneities in the stress field across the measured sample. Regardless of the number of layers, the stress uptake is zero at the edges of the flake. Similar behavior has been documented for the monolayer graphene,[41] and it indicates that at least up to a certain degree the stress is transferred to the graphene by a shear mechanism at the interface.

Another local feature depicted by the vertical black line on the monolayer part, which marks a very narrow region with a zero strain, is probably connected with a crack formation in the graphene flake (for additional data, see Supporting Information Figure S1).

As shown in Figure 4a, there is an obvious difference in the stress uptake between the mono- and bilayer parts in our sample, and this was also reflected (Figure 3b,d) in the observed differences at the onset of failure for the mono- and bilayer graphenes. In fact, since the bilayer has twice the thickness of the monolayer, it would require a much higher interface shear stress for the same level of axial strain transferred to the flakes. If the ceiling of the interface shear has been reached at 0.5% strain for the bilayer/PMMA system, then interface failure (or slippage) is quite likely to occur. This would certainly lead to the relaxation of the stress transferred to the flakes exactly as observed in Figure 3b,d.

dx.doi.org/10.1021/nl203565p | Nano Lett. 2012, 12, 687–693

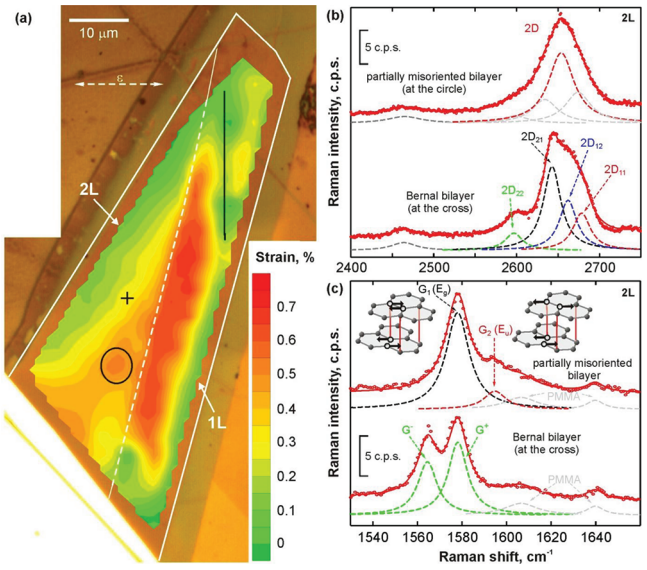

Figure 4. (a) Strain map of the flake F2 as calculated from Raman 2D band positions at a nominal tension of 0.74% (see Methods). Example spectra of the 2D (chart b) and G band regions (chart c) of the bilayer part measured inside the black circle and at the cross. Dashed curves are Lorentzian fits of the individual components with solid lines as their convolution, and the points represent original spectra.

We now turn our attention to local failure events throughout the large flake areas. In Figure.4a, the black ellipse marks a small region on the bilayer not larger than 5 μm close to the bilayer/monolayer boundary, where dramatic spectral changes are observed for the bilayer 2D band. This is in contrast to the rest of the specimen which exhibits the line shape common to the four peaks of a Bernal bilayer (bottom in Figure 4b) originating from the different electron−phonon scattering processes discussed above. The Raman signal from the marked region shows a 2D peak completely lacking the characteristic features of an AB stacked bilayer (top in Figure 4b) and has a line shape more typical of a monolayer or non-AB stacked bilayer (for other maps displaying additional information from the 2D band deconvolution, see Supporting Information Figure S2).[47] This might be due to cohesive (interplanar) shear failure in the bilayer due to the high normal stresses developing in that region due to the possible presence of atomic defects. The possibility of detecting cohesive failure in multilayer graphenes through the Bernal to non-Bernal transition opens the way for assessing failure at the nanoscale with the use of Raman spectroscopy.

The G band in the Raman spectra from this region of the sample shows a peculiar behavior as well (Figure 4c, top spectrum). In this flake, the prevalent G band shape of the strained bilayer (and the monolayer, too) consists of G^- and G^+ sub-bands with a G^-/G^+ intensity ratio of ∼0.65, centered on frequencies corresponding to the level of applied uniaxial deformation (Figure 4c, bottom).[23,26,29] However, in the labeled region, the G band exhibits one intense component (further noted as G_1), red-shifted to 1578 cm^{-1} from the zero strain position (∼1584 cm^{-1}), but also another weaker band (noted as G_2) at 1594 cm^{-1}, i.e., at a much higher wavenumber than could be expected taking into account the typical G^- and G^+ shift values.[24,26] The assignment of the G_1 and G_2 bands to the individual layers is highly improbable, since this would have to be accompanied by two clearly separated 2D bands (by ∼30 cm^{-1}). It also has to be noted that the presence of this weak band is strictly limited to the marked region and is always accompanied by the distorted 2D peak shape and a complete absence of the D band, which rules out the assignment of the G_2 band to the D′ band (see Figure S3 and related discussion in Supporting Information). This observation might suggest that the two graphene layers experience unequal strain fields, resulting in the inversion symmetry breaking of the bilayer lattice. In bilayer graphene the doubly degenerate E_{2g} branch of the monolayer evolves, at the Γ point, into two doubly degenerate branches E_g and E_u (insets in Figure 4c).[48] The antisymmetric E_u mode is under normal conditions Raman inactive and can be observed using infrared spectroscopy. The E_g and E_u modes were reported to split due to a weak interlayer coupling in gated[49−51] or chemically doped[52] bilayer graphene. It is tempting to assign the G_1 and G_2 band to E_g and E_u phonons, respectively. As mentioned above, the red-shift of the E_g (∼G_1) band is about 6 cm^{-1} from the zero strain position. Considering the ambient position of the E_u mode close to 1600 cm^{-1},[53] a similar shift can be ascribed to the G_2 band. The much weaker intensity of the E_u mode suggests that the degree of inversion-symmetry breaking is rather low, indicating only a mild mixing between the E_g and E_u modes.[54]

The peculiar G and 2D band features point to a local asymmetry between the two layers of the otherwise Bernal stacked bilayer graphene. This is in accordance with the recent theoretical work of Choi et al.,[20] who stated that transverse electric fields across the two layers can be generated without any external electronic sources, thereby opening an energy gap. With this respect, it should be stressed that even though the applied stress was uniaxial and very low (0.74%), our observation shows a relative simplicity of tuning the nonuniform strain fields in the two layers, which is perfectly in line with very recent calculations of Verberck et al.[55]

In summary, we present a systematic uniaxial deformation Raman study of several bilayer graphene samples (and monolayers being parts of the same flakes) embedded in a polymer matrix, using laser energies from the visible to the near-IR range. Our experimental data show that strain directly influences the double resonance bands, while the $2D_{11}$ component is more sensitive to the induced deformations. This work contributes an experimental insight into the various scenarios[23,29,36,38] presented in the recent literature regarding the relative contribution of the inner vis-à-vis the outer process to the 2D Raman peak.

In terms of the mechanical stability, we observed that the interface failure or slippage of the bilayer occurs at lower tension levels compared to the monolayer part of the same flake. Additionally, the Bernal-stacked two layers fully embedded in a matrix are locally susceptible to nonuniform strain field components, which induce a breaking of the bilayer inversion symmetry. This in turn leads to the activation of the infrared E_u mode and the appearance of a single broad 2D band component. The results can be explained considering the band gap opening, as proposed by recent theoretical predictions.[20,55] Further work toward a control, at a larger scale, of the strains applied independently to each of the two layers is needed to confirm the viability and the potential of such a mechanism.

■ ASSOCIATED CONTENT

Supporting Information

Materials and methods; crack mapping—D band appearance—in the monolayer part in flake F2; additional maps of the 2D

dx.doi.org/10.1021/nl203565p | Nano Lett. 2012, 12, 687−693

band deconvolution parameters; discussion on the origin of the G_1 and G_2 bands. This material is available free of charge via the Internet at http://pubs.acs.org.

AUTHOR INFORMATION

Corresponding Author

*E-mail: otakar.frank@jh-inst.cas.cz; kpapag@upatras.gr.

ACKNOWLEDGMENTS

FORTH/ICE-HT acknowledge financial support from the John S. Latsis Public Benefit Foundation (Greece). Part of this work has been funded by "Graphene Centre" of Foundation of Research and Technology Hellas. K.S.N. is grateful to the Royal Society and European Research Council (Grant 207354 - "Graphene") for support. O.F., M.B., and L.K. further acknowledge the financial support of Czech Ministry of Education Youth and Sports (Contract LC-510), the Academy of Sciences of the Czech Republic (Contracts IAA 400400804 and KAN 200100801), and the EC seventh FP project Molesol (256617). Finally, this research has been cofinanced by the ESF and Greek national funds through the Operational Program "Education and Lifelong Learning" of the NSRF - Research Funding Program: Heracleitus II.

REFERENCES

(1) Novoselov, K. S.; Geim, A. K.; Morozov, S. V.; Jiang, D.; Zhang, Y.; Dubonos, S. V.; Grigorieva, I. V.; Firsov, A. A. *Science* **2004**, *306*, 666.

(2) Geim, A. K. *Science* **2009**, *324*, 1530.

(3) Lee, C.; Wei, X. D.; Kysar, J. W.; Hone, J. *Science* **2008**, *321*, 385.

(4) Bunch, J. S.; van der Zande, A. M.; Verbridge, S. S.; Frank, I. W.; Tanenbaum, D. M.; Parpia, J. M.; Craighead, H. G.; McEuen, P. L. *Science* **2007**, *315*, 490.

(5) Frank, O.; Tsoukleri, G.; Riaz, I.; Papagelis, K.; Parthenios, J.; Ferrari, A. C.; Geim, A. K.; Novoselov, K. S.; Galiotis, C. *Nature Commun.* **2011**, *2*, 255.

(6) Sakhaee-Pour, A.; Ahmadian, M. T.; Vafai, A. *Solid State Commun.* **2008**, *147*, 336.

(7) Huang, X.; Qi, X.; Boey, F.; Zhang, H. *Chem. Soc. Rev.* **2012**, DOI: 10.1039/C1CS15078B.

(8) Ohta, T.; Bostwick, A.; Seyller, T.; Horn, K.; Rotenberg, E. *Science* **2006**, *313*, 951.

(9) Craciun, M. F.; Russo, S.; Yamamoto, M.; Oostinga, J. B.; Morpurgo, A. F.; Tarucha, S. *Nature Nanotechnol.* **2009**, *4*, 383.

(10) Zhang, Y. B.; Tang, T. T.; Girit, C.; Hao, Z.; Martin, M. C.; Zettl, A.; Crommie, M. F.; Shen, Y. R.; Wang, F. *Nature* **2009**, *459*, 820.

(11) Choi, S.-M.; Jhi, S.-H.; Son, Y.-W. *Phys. Rev. B* **2010**, *81*, 081407.

(12) Liu, F.; Ming, P. M.; Li, J. *Phys. Rev. B* **2007**, *76*, 064120.

(13) Mohr, M.; Papagelis, K.; Maultzsch, J.; Thomsen, C. *Phys. Rev. B* **2009**, *80*, 205410.

(14) Cocco, G.; Cadelano, E.; Colombo, L. *Phys. Rev. B* **2010**, *81*, 241412.

(15) Castro, E. V.; Novoselov, K. S.; Morozov, S. V.; Peres, N. M. R.; Dos Santos, J. M. B. L.; Nilsson, J.; Guinea, F.; Geim, A. K.; Neto, A. H. C. *Phys. Rev. Lett.* **2007**, *99*, 216802.

(16) Castro, E. V.; Novoselov, K. S.; Morozov, S. V.; Peres, N. M. R.; dos Santos, J. M. B. L.; Nilsson, J.; Guinea, F.; Geim, A. K.; Neto, A. H. C. *J. Phys.: Condens. Matter* **2010**, *22*, 175503.

(17) McCann, E.; Fal'ko, V. I. *Phys. Rev. Lett.* **2006**, *96*, 086805.

(18) Lee, S. H.; Chiu, C. W.; Ho, Y. H.; Lin, M. F. *Synth. Met.* **2010**, *160*, 2435.

(19) Nanda, B. R. K.; Satpathy, S. *Phys. Rev. B* **2009**, *80*, 165430.

(20) Choi, S.-M.; Jhi, S.-H.; Son, Y.-W. *Nano Lett.* **2010**, *10*, 3486.

(21) Mucha-Kruczynski, M.; Aleiner, I. L.; Fal'ko, V. I. *Phys. Rev. B* **2011**, *84*, 041404.

(22) Ferralis, N. *J. Mater. Sci.* **2010**, *45*, 5135.

(23) Frank, O.; Mohr, M.; Maultzsch, J.; Thomsen, C.; Riaz, I.; Jalil, R.; Novoselov, K. S.; Tsoukleri, G.; Parthenios, J.; Papagelis, K.; Kavan, L.; Galiotis, C. *ACS Nano* **2011**, *5*, 2231.

(24) Frank, O.; Tsoukleri, G.; Parthenios, J.; Papagelis, K.; Riaz, I.; Jalil, R.; Novoselov, K. S.; Galiotis, C. *ACS Nano* **2010**, *4*, 3131.

(25) Huang, P. Y.; Ruiz-Vargas, C. S.; van der Zande, A. M.; Whitney, W. S.; Levendorf, M. P.; Kevek, J. W.; Garg, S.; Alden, J. S.; Hustedt, C. J.; Zhu, Y.; Park, J.; McEuen, P. L.; Muller, D. A. *Nature* **2011**, *469*, 389.

(26) Mohiuddin, T. M. G.; Lombardo, A.; Nair, R. R.; Bonetti, A.; Savini, G.; Jalil, R.; Bonini, N.; Basko, D. M.; Galiotis, C.; Marzari, N.; Novoselov, K. S.; Geim, A. K.; Ferrari, A. C. *Phys. Rev. B* **2009**, *79*, 205433.

(27) Proctor, J. E.; Gregoryanz, E.; Novoselov, K. S.; Lotya, M.; Coleman, J. N.; Halsall, M. P. *Phys. Rev. B* **2009**, *80*, 073408.

(28) Tsoukleri, G.; Parthenios, J.; Papagelis, K.; Jalil, R.; Ferrari, A. C.; Geim, A. K.; Novoselov, K. S.; Galiotis, C. *Small* **2009**, *5*, 2397.

(29) Yoon, D.; Son, Y.-W.; Cheong, H. *Phys. Rev. Lett.* **2011**, *106*, 155502.

(30) Ferrari, A. C. *Solid State Commun.* **2007**, *143*, 47.

(31) Ferrari, A. C.; Meyer, J. C.; Scardaci, V.; Casiraghi, C.; Lazzeri, M.; Mauri, F.; Piscanec, S.; Jiang, D.; Novoselov, K. S.; Roth, S.; Geim, A. K. *Phys. Rev. Lett.* **2006**, *97*, 187401.

(32) Malard, L. M.; Pimenta, M. A.; Dresselhaus, G.; Dresselhaus, M. S. *Phys. Rep.* **2009**, *473*, 51.

(33) Tuinstra, F.; Koenig, J. L. *J. Chem. Phys.* **1970**, *53*, 1126.

(34) Maultzsch, J.; Reich, S.; Thomsen, C. *Phys. Rev. B* **2004**, *70*, 155403.

(35) Huang, M. Y.; Yan, H. G.; Chen, C. Y.; Song, D. H.; Heinz, T. F.; Hone, J. *Proc. Natl. Acad. Sci. U. S. A.* **2009**, *106*, 7304.

(36) Huang, M.; Yan, H.; Heinz, T. F.; Hone, J. *Nano Lett.* **2010**, *10*, 4074.

(37) Mohr, M.; Maultzsch, J.; Thomsen, C. *Phys. Rev. B* **2010**, *82*, 201409(R).

(38) Venezuela, P.; Lazzeri, M.; Mauri, F. *Phys. Rev. B* **2011**, *84*, 035433.

(39) Ding, F.; Ji, H.; Chen, Y.; Herklotz, A.; Dörr, K.; Mei, Y.; Rastelli, A.; Schmidt, O. G. *Nano Lett.* **2010**, *10*, 3453.

(40) Metzger, C.; Remi, S.; Liu, M.; Kusminskiy, S. V.; Castro Neto, A. H.; Swan, A. K.; Goldberg, B. B. *Nano Lett.* **2009**, *10*, 6.

(41) Gong, L.; Kinloch, I. A.; Young, R. J.; Riaz, I.; Jalil, R.; Novoselov, K. S. *Adv. Mater.* **2010**, *22*, 2694.

(42) Young, R. J.; Gong, L.; Kinloch, I. A.; Riaz, I.; Jalil, R.; Novoselov, K. S. *ACS Nano* **2011**, *5*, 3079.

(43) Cançado, L. G.; Reina, A.; Kong, J.; Dresselhaus, M. S. *Phys. Rev. B* **2008**, *77*, 245408.

(44) Malard, L. M.; Nilsson, J.; Elias, D. C.; Brant, J. C.; Plentz, F.; Alves, E. S.; Neto, A. H. C.; Pimenta, M. A. *Phys. Rev. B* **2007**, *76*, 201401.

(45) Nicolle, J.; Machon, D.; Poncharal, P.; Pierre-Louis, O.; San-Miguel, A. *Nano Lett.* **2011**, *11*, 3564.

(46) Mafra, D. L.; Moujaes, E. A.; Doorn, S. K.; Htoon, H.; Nunes, R. W.; Pimenta, M. A. *Carbon* **2011**, *49*, 1511.

(47) Poncharal, P.; Ayari, A.; Michel, T.; Sauvajol, J. L. *Phys. Rev. B* **2008**, *78*, 113407.

(48) Yan, J. A.; Ruan, W. Y.; Chou, M. Y. *Phys. Rev. B* **2008**, *77*, 125401.

(49) Bruna, M.; Borini, S. *Phys. Rev. B* **2010**, *81*, 125421.

(50) Gava, P.; Lazzeri, M.; Saitta, A. M.; Mauri, F. *Phys. Rev. B* **2009**, *80*, 155422.

(51) Malard, L. M.; Elias, D. C.; Alves, E. S.; Pimenta, M. A. *Phys. Rev. Lett.* **2008**, *101*, 257401.

(52) Zhang, W.; Lin, C.-T.; Liu, K.-K.; Tite, T.; Su, C.-Y.; Chang, C.-H.; Lee, Y.-H.; Chu, C.-W.; Wei, K.-H.; Kuo, J.-L.; Li, L.-J. *ACS Nano* **2011**, *5*, 7517.

(53) Kuzmenko, A. B.; Benfatto, L.; Cappelluti, E.; Crassee, I.; van der Marel, D.; Blake, P.; Novoselov, K. S.; Geim, A. K. *Phys. Rev. Lett.* **2009**, *103*, 116804.

(54) Yan, J.; Villarson, T.; Henriksen, E. A.; Kim, P.; Pinczuk, A. *Phys. Rev. B* **2009**, *80*, 241417(R).
(55) Verberck, B.; Partoens, B.; Peeters, F. M.; Trauzettel, B. arXiv e-Print archive 2011, *arXiv*:1111.4957v1 [cond-mat.mtrl-sci].

NOTE ADDED AFTER ASAP PUBLICATION

This article was published ASAP on December 22, 2011. Figure 2 has been enlarged for clarity. The revised version was posted on January 4, 2012.

Phys. Status Solidi B **253,** No. 12, 2355–2361 (2016) / **DOI** 10.1002/pssb.201600233

physica status solidi b
www.pss-b.com
basic solid state physics

Stress and charge transfer in uniaxially strained CVD graphene

Milan Bousa[*,1,2], George Anagnostopoulos[3], Elena del Corro[1], Karolina Drogowska[1], Jan Pekarek[4], Ladislav Kavan[1,2], Martin Kalbac[1], John Parthenios[3], Konstantinos Papagelis[3], Costas Galiotis[3,5], and Otakar Frank[1]

[1] J. Heyrovsky Institute of Physical Chemistry of the AS CR v.v.i., Dolejskova 2155/3, CZ 182 23 Prague 8, Czech Republic
[2] Faculty of Science, Department of Inorganic Chemistry, Charles University in Prague, Albertov 6, CZ 128 43 Prague 2, Czech Republic
[3] Institute of Chemical Engineering Sciences, Foundation for Research and Technology − Hellas (FORTH/ICE-HT), P.O. Box 1414, 265 04 Patras, Greece
[4] Faculty of Electrical Engineering and Communication, Centre of Sensors, Information and Communication Systems, Brno University of Technology, Technicka 3058/10, CZ 616 00 Brno, Czech Republic
[5] Department of Chemical Engineering, University of Patras, 26504 Patras, Greece

Received 15 April 2016, revised 20 June 2016, accepted 27 June 2016
Published online 20 July 2016

Keywords chemical vapour deposition, graphene, Raman spectroscopy, uniaxial tension

[*] Corresponding author: e-mail milan.bousa@jh-inst.cas.cz, Phone: +420 266 053 955, Fax: +420 286 582 307

Mechanical properties of graphene prepared by chemical vapour deposition (CVD) are not easily comparable to the properties of nearly perfect graphene prepared by mechanical cleavage. In this work, we attempt to investigate the mechanical performance of CVD graphene (simply supported or embedded in polymer matrix), transferred by two different techniques, under uniaxial loading with simultaneous *in situ* monitoring by Raman microspectroscopy. The level of charge transfer doping and strain is assessed using the vector analysis modified for uniaxial strain. The strain distribution across the samples varies significantly, owing to the growth and transfer process, which induces wrinkles and faults in the CVD graphene. In simply supported specimens, the stress transfer efficiency is generally very low and the changes in Raman spectra are dominated by variations in the charge transfer originating from the realignment of the domains on the substrate upon the application of strain. In contrast, samples covered with an additional polymer layer exhibit an improved stress transfer efficiency, and the alterations of charge doping levels are negligible. In fully embedded specimens, the variations in stress transfer efficiencies are caused by the size of the effective graphene domains defined by cracks, folds and/or wrinkles.

© 2016 WILEY-VCH Verlag GmbH & Co. KGaA, Weinheim

1 Introduction The presence of strain [1] and substrate-induced charge transfer doping [2] in graphene requires reliable methods for their monitoring and correct evaluation. Both strain and doping are known to alter the electronic structure of graphene, intentionally [3] as well as accidentally [4]. Hence, the ability to correctly assess and discriminate strain and doping in graphene and graphene-based devices is of utmost importance.

Raman spectroscopy has been established as a work horse for a swift and non-destructive analysis of graphene-related materials, providing not only basic characterisation in terms of the layer number or disorder in the samples, but also a more detailed information about the levels of doping or strain [5, 6]. Nevertheless, when these two effects intermix, such an analysis can become very difficult. A method using the correlation of the G and 2D peak frequencies (Pos(G) and Pos(2D), respectively) has been introduced [7] and successfully tested recently [8–11] to separate biaxial strain from charge doping in various graphene samples. This approach, based on a vector analysis of the data points in the Pos(G)–Pos(2D) space, is relatively simple to conduct in certain well-defined cases, but the interpretation of the results has to be performed carefully when the experimental conditions deviate from the above mentioned biaxial strain–uniform doping situation. In that case, to monitor the changes in the system, other parameters of the G and 2D peaks have to be analysed, such as their widths (further defined as full width at half-maxima,

© 2016 WILEY-VCH Verlag GmbH & Co. KGaA, Weinheim

FWHM), or their intensity ratio [8]. Alternatively, another Raman feature, such as the 2D' peak can be included to provide more accuracy in the analysis [12].

The G peak corresponds to a first order Raman scattering process with a phonon of almost zero momentum. It is associated with the in-plane, doubly degenerate phonon from the transverse optical (TO) and longitudinal optical (LO) branches with E_{2g} symmetry at the Brillouin zone (BZ) centre (Γ point) [13]. Both frequency and width of the G mode are strongly influenced by the presence of doping [14, 15] and the application of stress [1, 16]. The increase of Pos(G) in both electron- and hole-doped graphene is caused by a non-adiabatic removal of the Kohn anomaly at Γ point [17], and the simultaneous decrease of FWHM(G) is caused by the Pauli blocking of phonon decay into electron–hole pairs. In general, strain causes G peak downshift under tension and upshift under compression with a rate of $\sim 62\,\mathrm{cm}^{-1}/\%$ for biaxial tension [18]. Under uniaxial strain the G peak splits into two components, G^- and G^+, with the shift rates of ~ -31 and $-10\,\mathrm{cm}^{-1}/\%$, respectively, for graphene on polymer substrates [19, 20], or of ~ -37 and $-19\,\mathrm{cm}^{-1}/\%$, respectively, for suspended graphene [21].

The 2D mode originates from a second-order triple resonant process between non-equivalent K points in graphene BZ, involving two zone-boundary, TO-derived phonons with opposite momenta [22, 23]. As shown recently, the 2D peak in suspended graphene is not fully symmetrical [24], which is even more pronounced in strained samples [25–28]. In a simplified one-dimensional picture of the 2D mode origin there are two dominant directions of the contributing phonon wavevectors – along K–Γ (so called inner) or K–M (outer) symmetry lines. Recent studies show a greater contribution of the inner processes [22, 25, 26, 29]. Nevertheless, a full two-dimensional description of the electronic peaks, phonon dispersion and matrix elements [22] has shown that the notation of inner or outer phonons is of a weaker relevance [28]. The 2D mode is dispersive, and its frequency changes with the excitation energy (E_L) with the slope $\partial\mathrm{Pos(2D)}/\partial E_L \sim 100\,\mathrm{cm}^{-1}\,\mathrm{eV}^{-1}$ [6]. The 2D peak is also sensitive to doping and mechanical stress but these effects manifest themselves differently from those of the G peak [1]. Strain causes the 2D peak shift in the same direction as the G peak, with the shift rates for biaxial strain larger by a factor of $\sim$2.2–2.5 [18, 30, 31]. Broadening and splitting of the 2D peak under uniaxial strain is very different to that of the G peak [25], but no such effects are observed for biaxial deformation [31]. Hole doping causes increase of Pos(2D) with a $\partial\mathrm{Pos(2D)}/\partial\mathrm{Pos(G)} \sim 0.5$–$0.7$ [7, 14, 32], whereas electron doping causes only a negligible Pos(2D) change for $n \leq 2 \times 10^{13}\,\mathrm{cm}^{-2}$ followed by a non-linear Pos(2D) decrease for higher n-doping levels [14, 32]. FWHM(2D) increases upon both p- and n-doping mainly due to electron–electron interactions, and also electron–phonon coupling strength [22, 33].

The effect of the grain size on the stress transfer was reported for mechanically exfoliated graphene, showing that a critical dimension of approximately 4 μm (parallel with the strain axis), is needed to achieve a full transfer of the applied strain from the substrate to the interior of the flake [34–36]. The strain-induced behaviour of CVD graphene is much less explored [37, 38], and the influence of absolute grain sizes is taken over by the wrinkles, which effectively rule the stress transfer, or rather the lack thereof, in this case [37]. The shift rate of 2D peak with strain was less than 25% of the shift rate corresponding to a full stress transfer ($\sim 60\,\mathrm{cm}^{-1}/\%$), in spite of the flake being covered by an additional polymer layer [37]. The analysis of the G peak was not possible due to intense overlapping peaks originating from the poly(ethylene terephthalate) (PET) substrate.

In the present work, we have focused on the separation of the effects of strain and doping in the Raman spectra of uniaxially strained CVD graphene prepared by two different transfer methods: (i) with separated grains introduced intentionally using an elastomer sacrificial layer (polyisobutylene, PIB) and (ii) the standard poly(methyl-methacrylate) (PMMA) technique. Apart from confirming the influence of grain sizes, both absolute and 'wrinkle-limited', we have shown the applicability of the strain-doping separation method also for uniaxially strained graphene samples.

2 Methods Graphene was grown on copper foils by low-pressure CVD as detailed in Ref. [39]. Alternatively, single layer graphene produced by CVD method and grown on copper foil supplied by AIXTRON Ltd. was used in the experiments.

The samples were transferred either by the dry transfer method using PIB as support polymer [40] or the standard PMMA method [41]. Scanning Electron Microscopy (SEM) images of the samples transferred by the two methods are shown in Fig. 1. The images were acquired using a HR-SEM Hitachi S4800 and a LEO SUPRA 35 VP scanning electron microscopes. In the case of PIB-assisted transfer, the SEM images were obtained in samples transferred to Si substrate due to a lower conductivity of the monolayer caused by the fragmentation during transfer.

As the target substrate for tensile experiments, clean and flexible PMMA beams of 3 mm thickness were used. They were previously spin coated with different polymers, SU8 photoresist (SU8 2000.5, MicroChem) or PMMA (3% in anisole, MicroChem). After the graphene transfer, some of the samples were covered by parylene C (120 nm thickness) or PMMA, in order to improve the strain transfer efficiency from the flexible substrate to the graphene flake. Further in text, the uncovered samples are denoted as simply supported and the covered ones as fully supported. Tensile strain in the graphene was imposed through a cantilever beam [19] or a four-point bending device [36]. In both cases, the strain response was monitored *in situ* using a micro-Raman setup with a 100× objective (N.A. = 0.9) (InVia Reflex, Renishaw or LabRAM HR, Horiba), and 514.5 nm (2.41 eV) or 632.8 nm (1.96 eV) excitation laser. The laser power was kept below 1.5 mW to avoid laser-induced heating. Typical spectra of single layer CVD graphene, as transferred onto SU8 and strained, are plotted in Fig. 2.

© 2016 WILEY-VCH Verlag GmbH & Co. KGaA, Weinheim

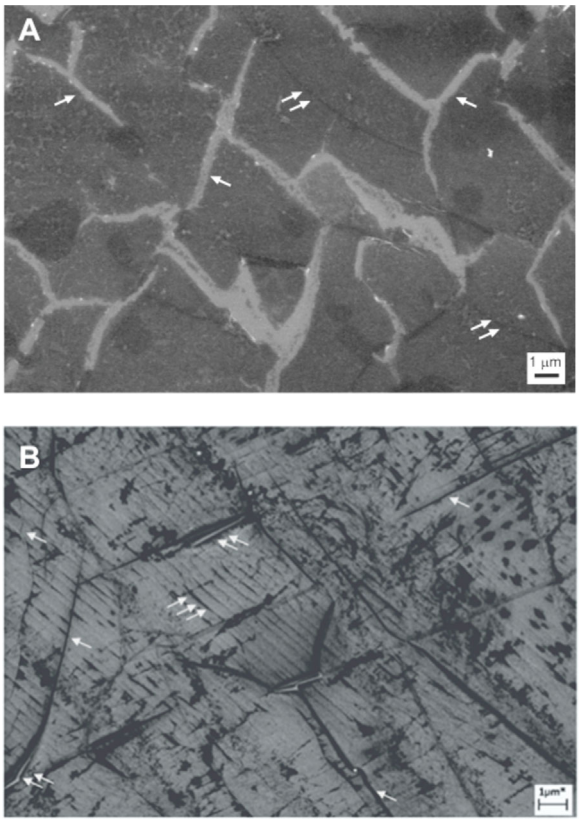

Figure 1 SEM images of the CVD graphene samples transferred by PIB (A; on Si) and PMMA (B; on SU8). The scale bar is 1 μm.

3 Results Figures 2 and 3 show the evolution of the monolayer graphene flake covered by parylene under uniaxial strain. In the Raman spectra (Fig. 2), downshifts of both the G and 2D peaks of graphene are visible in the spectrum strained to $\varepsilon_m = 0.5\%$. The Raman peaks of the polymers do not shift with strain. The measurement was done using incident laser polarisation parallel to the strain

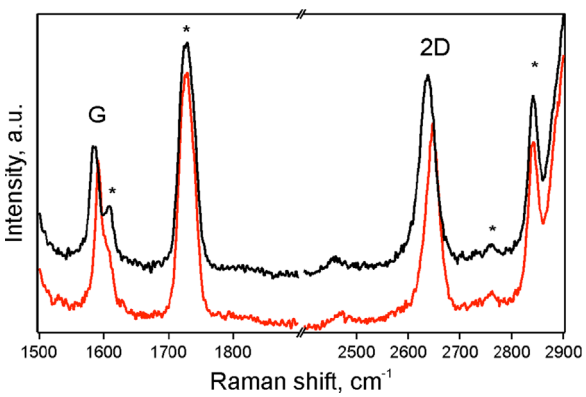

Figure 2 Raman spectra of CVD graphene embedded between two polymer layers (SU8 at the bottom, parylene C on top) at 0 (red line) and 0.5% (black line) of nominal strain. Raman peaks of the polymer are marked by asterisks. Laser excitation energy was 1.96 eV.

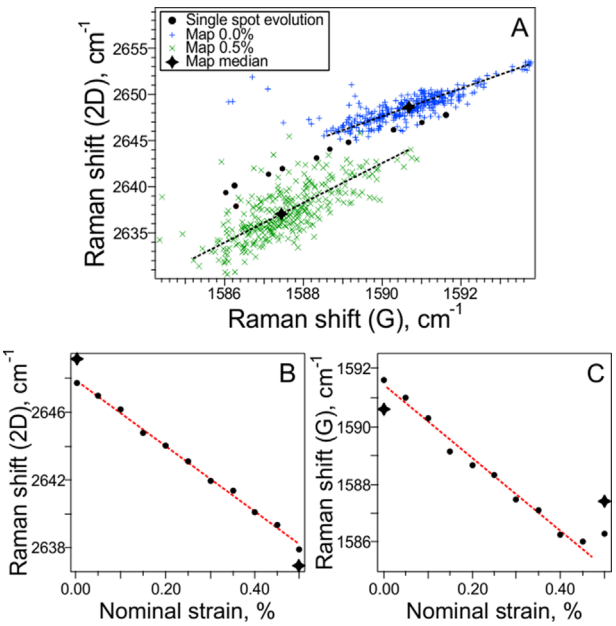

Figure 3 Evolution of G and 2D peaks in the PIB-transferred, fully supported sample: (A) data points from large area mapping (0% – blue, 0.5% – green) with stars as their medians and full lines as least-squares line fits, black points follow the evolution on a single spot with 0.05% step, which is then detailed individually in (B) and (C) for the evolution of 2D and G peaks with strain. Laser excitation energy was 1.96 eV.

axis; no selection of the scattered light polarisation (via an 'analyzer') was employed. The graphene Raman peaks thus correspond to a sum of signals from all scattered polarisation directions and the shift rates can be taken from single Lorentzian shapes fitted to the Raman peaks. The evolution of the Raman shifts of the G and 2D peaks with strain is plotted in Fig. 3c and b, with their shift rates being 12.7 and 19.4 cm^{-1}/%, respectively. In the case of the 2D peak (Fig. 3b), the data points lie on a line, whereas the G peak data points are markedly more scattered and its position at 0.5% strain is even increased compared to the previous step (note, the shift rate is, therefore, calculated only between 0 and 0.45% of strain). The erratic behaviour of the G peak compared to the smooth evolution of the 2D peak is a first indication of another influence on the Raman spectra apart from the strain. A second indication comes from the shift rates. Compared to the theoretical peak shifts (~65 cm^{-1}/% for the 2D peak and ~21.5 cm^{-1}/% for the G peak), we can see a serious discrepancy in the ratios between the measured and theoretical values: a factor of ~0.33 and 0.59 for the 2D and G peaks, respectively. Note that the theoretical G band shift is the average of the shift rates for G^+ and G^- [1].

Both above mentioned observations – the discrepancy between the measured and theoretical values of the G and 2D peaks and the scatter of the G peak Raman shifts – can be explained by doping. The variations in the G peak position can be rationalised by the presence of spatial fluctuations of

© 2016 WILEY-VCH Verlag GmbH & Co. KGaA, Weinheim

carrier concentrations, sometimes termed as charge puddles [42], and by their fluctuation caused by the strain-induced changes in the graphene–substrate interactions. The different ratios of the G and 2D peak shifts with respect to the theoretical values can reflect a continuous change in the doping level, which influences more the G peak shift. Hence, the strain shift rates should be checked and adjusted (if needed) using the vector separation method to account for the different shifts caused by strain and doping (Fig. 3a). Apart from the point at $\varepsilon_m = 0.5\%$ strain, the evolution of the G and 2D Raman shifts at the single-spot (Fig. 3a) can be fitted by a line with the slope of ~1.5. This value indicates a substantial influence from changes in doping. We apply the vector analysis using the slope for strain (i.e. iso-doping) line of three obtained from the average peak shifts for uniaxial strain in fully supported graphene [1] and the slope for hole doping of 0.7 [7] and subsequently quantify the data using the above mentioned shift rates for strain and a simplified formula for doping estimation $\Delta\mathrm{Pos(G)} = -0.986n^2 + 9.847n$ ($10^{13}\,\mathrm{cm}^{-2}$) [8], where n is the carrier concentration. We obtain $\Delta n \sim -0.37 \times 10^{13}\,\mathrm{cm}^{-2}$. The corresponding adjusted G peak strain shift rate is $4.3\,\mathrm{cm}^{-1}/\%$, amounting to ~0.2 of the theoretical shift rates.

As can be seen, even a small change in the doping level can lead to considerable changes in the quantified strain. The decrease in carrier concentration (dedoping) observed during the single-spot measurement is, however, counterintuitive. In general, such lower carrier concentration should be accompanied also by a loss of adhesion to the substrate, which in turn would be reflected in smaller Raman shifts of both G and 2D peak per strain step. Nevertheless, the Raman shifts – especially of the 2D peak – show a linear evolution in the whole experiment (Fig. 3b and c). It can be hypothesised that the laser spot was located in a graphene grain (charge puddle) with a higher p-doping level than the rest of sample and by flattening out the graphene's surface during the tensile test, the charge has been distributed along the neighbouring grains. Indeed, the data points acquired in maps taken at 0% and 0.5% of nominal strain (Fig. 3b) clearly evidence that the behaviour in the one spot randomly selected to follow the stretching experiment shows an anomalous evolution compared to the bulk of the data. The medians of the distributions lie on a line with a slope of ~3.6, indicating that even a minor overall increase in the net doping took place. The increased doping level is expected due to an increasing contact between graphene and the substrate. The vector analysis performed on the medians yields the strain G peak shift rate of $\sim 8.9\,\mathrm{cm}^{-1}/\%$ and Δn of $\sim 0.10 \times 10^{13}\,\mathrm{cm}^{-2}$, giving the ratio to the theoretical strain shift rate of 0.44. The ratio is higher than the one previously measured for CVD graphene on a different system with a PET as the bottom and PMMA as the top substrate [37]. If the 2D peak shift would be compared without adjusting for the doping effects, the ratio to the theoretical shift rate would give 0.38 in our case. We can also see that the distributions of the map points in Fig. 3a changed their orientation: from 1.5 at 0% to 2.2 at 0.5% indicating again that upon tension

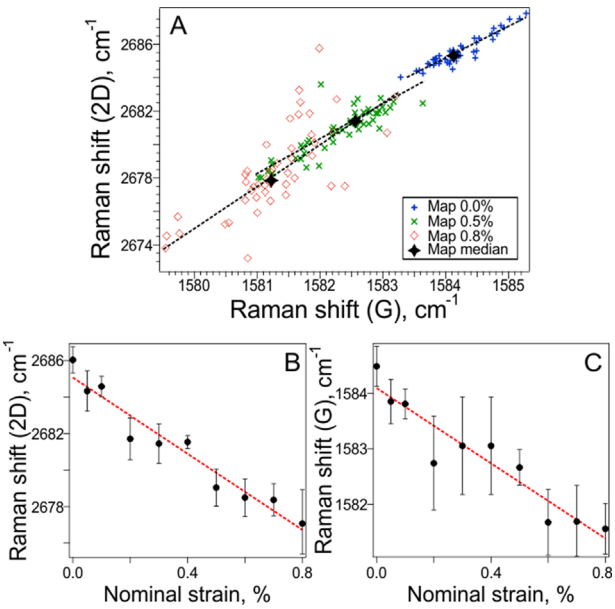

Figure 4 Evolution of G and 2D peaks in the PMMA-transferred, fully supported sample: (A) data points from large area mapping (0% – blue, 0.5% – green, 0.8% – red) with stars as their medians and full lines as least-squares line fits; (B) and (C) show the evolution of 2D and G peaks with strain. Laser excitation energy was 2.41 eV.

the doping levels are equalised, whereas the differences between the points are dominated by strain.

The case of the fully supported CVD monolayer transferred by PMMA is depicted in Fig. 4. The distribution of the mapping points changes its orientation from 1.9 to almost 2.6 at 0.8% of nominal strain (Fig. 4a), indicating the increased domination of strain. The average shift rates of the 2D and G peaks (Fig. 4b and c) are 10.4 and $3.4\,\mathrm{cm}^{-1}/\%$, respectively, and their ratio ~3.1 showing a minor increase in net doping level. After an adjustment of those doping effects, the G peak shift rate increases to $3.6\,\mathrm{cm}^{-1}/\%$ and the overall ratio to the theoretical shift rate is 0.17.

The reasons for difference in the shift rates between the PIB- and PMMA-transferred samples can be attributed to the effective grain sizes. The polymer-assisted transfer induces all kinds of disorder and inhomogeneities to the sample, mostly due to a larger area of the graphene film compared to the copper surface, and large surface tension when dissolving the polymer. The most common features thus formed are tears or cracks, individual folds or periodic wrinkles. In Fig. 1, we can see a marked difference between the two samples. While the PIB-transferred one shows predominantly cracks and folds, the PMMA transfer retains a much better continuity of the film, but induces many wrinkles. When we measure the mean sizes of individual graphene domains separated by either of those discontinuities, we get ~2 μm for PIB transfer and less than ~0.5 μm for PMMA transfer. The larger effective domain size of the PIB-transferred samples is then reflected in the higher strain transfer efficiency.

© 2016 WILEY-VCH Verlag GmbH & Co. KGaA, Weinheim

Table 1 Raman peak widths for PIB- and PMMA-transferred, fully supported samples.

	strain[a] (%)	FWHM(G)[b] (cm^{-1})	FWHM(2D)[b] (cm^{-1})
PIB	0.00	8.9 ± 0.8	31.2 ± 0.9
	0.22	11.6 ± 1.2	33.8 ± 1.5
PMMA	0.00	15.7 ± 0.9	30.2 ± 0.7
	0.14	18.6 ± 0.8	33.8 ± 2.4

[a]The real strain, calculated by multiplying the stress transfer efficiency and the maximum achieved nominal strain ε_m [12].
[b]Average values $\pm$ standard deviation obtained from Raman maps.

Let us now discuss the differences between the two above mentioned cases from the viewpoint of Raman peak widths. The mean values of FWHMs of the G and 2D peaks at zero and maximum achieved strain for both the PIB- and PMMA-transferred samples are given in Table 1.

In general, three major effects are responsible for changes in the Raman peak widths in monolayer graphene. Both G and 2D peaks broaden and eventually split into two (G peak) or more (2D peak) components with increasing uniaxial strain due to symmetry lowering [1]. The G peak broadening (splitting) follows a monotonic trend (in the case when scattered light with all polarisation directions is registered), whereas the evolution of the 2D peak width with uniaxial strain is more complicated, non-linear and also dependent on the laser excitation energy [25]. Charge doping induces narrowing of the G peak (already at small doping levels) and broadening of the 2D peak (more pronounced for higher doping levels); neither of the effects being linear [15]. And finally, broadening of both peaks can be caused by disorder, stemming either from structural defects [43] and/or from random fluctuations of strain and doping within the laser spot [44]. As can be seen, the peak widths represent an intricate superposition of several factors, especially if uniaxial strain is present, therefore, the interpretation of FWHM values has a limited usage. However, several simple assumptions can be made comparing the numbers in Table 1 and the peak shifts from Figs. 3 and 4 and the discussion thereof. At zero strain level, the small FWHM(G) of the PIB-transferred sample shows a high doping level. The FWHM(G) of the PMMA-transferred sample is significantly higher, and thus smaller doping can be expected. In the same time, the FWHM(2D) of the two samples is larger than 30 cm^{-1} and alike within the error margin. This indicates that apart from differences in doping [15], also varying amount of disorder [44] can be traced between the two samples. As the D band intensity is very small in both cases, the main source of disorder comes from strain/doping fluctuation in the laser spot. In the PIB sample at zero strain, the main source of 2D peak broadening comes from doping, while in the PMMA sample, the broadening originates in nanoscale strain/doping fluctuations. The latter conclusion is also in line with the much higher density of discontinuities like folds or wrinkles in the PMMA sample, as discussed above.

Upon uniaxial loading, both peaks broaden in both sample types. However, we shall consider only the evolution of the G peak width due to the complicated nature of 2D peak broadening. The theoretical rate of G peak splitting with uniaxial strain is $\sim$21 cm^{-1}/%, a value almost identical to the average shift rate of the two components ($\sim$20.5 cm^{-1}/%). Hence, at smaller strains, where the two components are strongly overlapping and not discernible, one can expect the rate of G peak broadening as a function of G peak shift, ΔFWHM(G)/ΔPos(G), of ~ -1. While the G peak evolution of the PMMA-transferred sample follows exactly this trend, ΔFWHM(G)/ΔPos(G) in the PIB sample reaches only -0.83. The difference can be caused either by decreasing disorder in the PIB sample, or more likely – in accordance with the results obtained from the vector analysis – by a small increase of the doping level in the PIB sample, which would slightly counterbalance the strain-induced broadening. As a final note, the different doping level in the initial state of the samples seems to be reflected also in the stress-transfer efficiency – a better contact between the sample and the substrate(s) would lead to a higher doping level as well as to a better stress transfer.

As another example of the usefulness of the vector analysis, a simply supported PIB-transferred CVD graphene was tested. In this case, the evolution of the G and 2D peaks in one spot shows a completely different scenario, where the frequency of the 2D peak decreases, while the G peak frequency increases (Fig. 5b and c). Such a behaviour can be explained only by a commanding

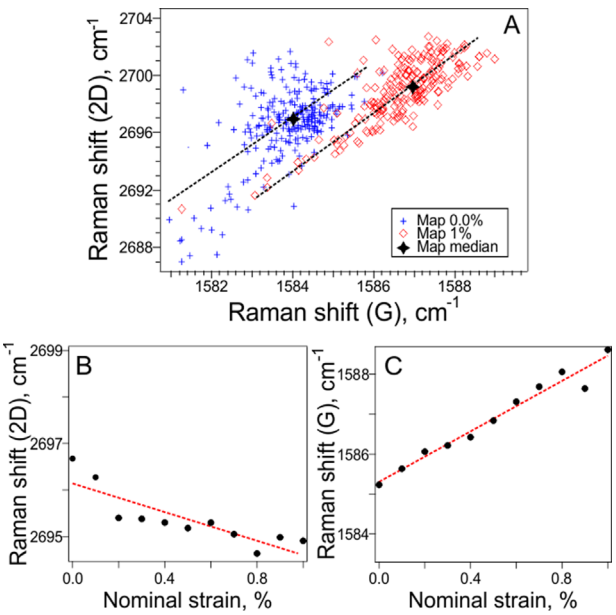

Figure 5 Evolution of G and 2D peaks in the PIB-transferred, simply supported sample: (A) data points from large area mapping (0% – blue, 1.0% – red) with stars as their medians and full lines as least-squares line fits; (B) and (C) show the evolution of 2D and G peaks with strain on a single spot. Laser excitation energy was 1.96 eV.

© 2016 WILEY-VCH Verlag GmbH & Co. KGaA, Weinheim

change in the doping level ($\Delta n \sim 0.27 \times 10^{13}\,\mathrm{cm}^{-2}$) with a minor contribution of a tensile strain (ratio to the theoretical shift rates of ~0.01). On top of that, the large spread of the values from the linear fit evidences substantial heterogeneities into the laser spot. The statistical evaluation in a larger area documents a slightly different overall evolution, which is dominated even more strongly by an increased doping level, where the medians of the two groups of data points are connected by a line with a slope of 0.7. Hence, during the experiment, most of the area of the sample experiences only a better alignment along the substrate, thereby increasing the doping level, and only in a few points the graphene is pinned to the substrate causing a minor interfacial stress transfer.

4 Conclusions We have shown the usability of vector analysis, performed on data points acquired by analysing the Raman G and 2D peak positions in graphene, to separate effects of strain and charge transfer doping in uniaxially strained CVD graphene samples. In all examined cases, uniaxial strain causes alignment of the graphene monolayer on the substrate resulting in an increase of doping level, however, only specimens covered by an additional polymer layer exhibit a certain amount of interfacial stress transfer. Its level is defined by the size of the effective graphene domains, which are separated by any kind of cracks, folds or wrinkles. The stress transfer efficiency is found to be ~44% for PIB-transferred graphene with domain sizes of ~2 μm and ~17% for PMMA-transferred sample with domain sizes of ~0.5 μm. A qualitative study of the G and 2D peak widths supports the conclusions from the vector analysis. It is also worth noting that single spot analysis can lead to misleading interpretation, as the samples display large strain variations and/or doping inhomogeneities. Therefore, a larger area Raman mapping has to be conducted and evaluated to provide quantifiable information about the real strain and doping levels induced by the arrangement and flattening of the domains upon loading.

Acknowledgements This project has received funding from the European Union's Horizon 2020 research and innovation programme under grant agreement no. 696656–GrapheneCore1. O.F., M.B and E.d.C. acknowledge the support of Czech Science Foundation project no. 14-15357S and M.K. acknowledges the support from ERC-CZ project no. LL1301. J.Pe. acknowledges the support by the project of National Sustainability Program under grant LO1401 of SIX Research Centre. Also, G.A., J.Pa., K.P. and C.G. acknowledge the financial support of, 'Tailor Graphene' ERC Advanced Grant (no. 321124) and the programme 'Graphene physics in the time domain and applications to 3D optical memories', Aristeia II (no. 4470).

References

[1] C. Galiotis, O. Frank, E. N. Koukaras, and D. Sfyris, Annu. Rev. Chem. Biomol. Eng. **6**, 121 (2015).
[2] Y. Shi, X. Dong, P. Chen, J. Wang, and L.-J. Li, Phys. Rev. B **79**, 115402 (2009).
[3] M. A. Bissett, M. Tsuji, and H. Ago, Phys. Chem. Chem. Phys. **16**, 11124 (2014).
[4] N. J. G. Couto, D. Costanzo, S. Engels, D.-K. Ki, K. Watanabe, T. Taniguchi, C. Stampfer, F. Guinea, and A. F. Morpurgo, Phys. Rev. X **4**, 041019 (2014).
[5] A. C. Ferrari and D. M. Basko, Nature Nanotechnol. **8**, 235 (2013).
[6] L. M. Malard, M. A. Pimenta, G. Dresselhaus, and M. S. Dresselhaus, Phys. Rep. **473**, 51 (2009).
[7] J. E. Lee, G. Ahn, J. Shim, Y. S. Lee, and S. Ryu, Nature Commun. **3**, 1024 (2012).
[8] O. Frank, J. Vejpravova, V. Holy, L. Kavan, and M. Kalbac, Carbon **68**, 440 (2014).
[9] F. Fromm, P. Wehrfritz, M. Hundhausen, and T. Seyller, New J. Phys. **15**, 113006 (2013).
[10] T. G. A. Verhagen, K. Drogowska, M. Kalbac, and J. Vejpravova, Phys. Rev. B **92**, 125437 (2015).
[11] J. Vejpravova, B. Pacakova, J. Endres, A. Mantlikova, T. Verhagen, V. Vales, O. Frank, and M. Kalbac, Sci. Rep. **5**, 15061 (2015).
[12] E. del Corro, L. Kavan, M. Kalbac, and O. Frank, J. Phys. Chem. C **119**, 25651 (2015).
[13] F. Tuinstra and J. L. Koenig, J. Chem. Phys. **53**, 1126 (1970).
[14] A. Das, S. Pisana, B. Chakraborty, S. Piscanec, S. K. Saha, U. V. Waghmare, K. S. Novoselov, H. R. Krishnamurthy, A. K. Geim, A. C. Ferrari, and A. K. Sood, Nature Nanotechnol. **3**, 210 (2008).
[15] O. Frank, M. S. Dresselhaus, and M. Kalbac, Acc. Chem. Res. **48**, 111 (2015).
[16] R. J. Young, I. A. Kinloch, L. Gong, and K. S. Novoselov, Compos. Sci. Technol. **72**, 1459 (2012).
[17] M. Lazzeri and F. Mauri, Phys. Rev. Lett. **97**, 266407 (2006).
[18] C. Androulidakis, E. N. Koukaras, J. Parthenios, G. Kalosakas, K. Papagelis, and C. Galiotis, Sci. Rep. **5**, 18219 (2015).
[19] O. Frank, G. Tsoukleri, J. Parthenios, K. Papagelis, I. Riaz, R. Jalil, K. S. Novoselov, and C. Galiotis, ACS Nano **4**, 3131 (2010).
[20] T. M. G. Mohiuddin, A. Lombardo, R. R. Nair, A. Bonetti, G. Savini, R. Jalil, N. Bonini, D. M. Basko, C. Galiotis, N. Marzari, K. S. Novoselov, A. K. Geim, and A. C. Ferrari, Phys. Rev. B **79**, 205433 (2009).
[21] I. Polyzos, M. Bianchi, L. Rizzi, E. N. Koukaras, J. Parthenios, K. Papagelis, R. Sordan, and C. Galiotis, Nanoscale **7**, 13033 (2015).
[22] P. Venezuela, M. Lazzeri, and F. Mauri, Phys. Rev. B **84**, 035433 (2011).
[23] J. Maultzsch, S. Reich, and C. Thomsen, Phys. Rev. B **70**, 155403 (2004).
[24] S. Berciaud, X. Li, H. Htoon, L. E. Brus, S. K. Doorn, and T. F. Heinz, Nano Lett. **13**, 3517 (2013).
[25] O. Frank, M. Mohr, J. Maultzsch, C. Thomsen, I. Riaz, R. Jalil, K. S. Novoselov, G. Tsoukleri, J. Parthenios, K. Papagelis, L. Kavan, and C. Galiotis, ACS Nano **5**, 2231 (2011).
[26] M. Huang, H. Yan, T. F. Heinz, and J. Hone, Nano Lett. **10**, 4074 (2010).
[27] D. Yoon, Y.-W. Son, and H. Cheong, Phys. Rev. Lett. **106**, 155502 (2011).

© 2016 WILEY-VCH Verlag GmbH & Co. KGaA, Weinheim

[28] R. Narula, N. Bonini, N. Marzari, and S. Reich, Phys. Rev. B **85**, 115451 (2012).
[29] V. N. Popov and P. Lambin, Carbon **54**, 86 (2013).
[30] K. Filintoglou, N. Papadopoulos, J. Arvanitidis, D. Christofilos, O. Frank, M. Kalbac, J. Parthenios, G. Kalosakas, C. Galiotis, and K. Papagelis, Phys. Rev. B **88**, 045418 (2013).
[31] J. Zabel, R. R. Nair, A. Ott, T. Georgiou, A. K. Geim, K. S. Novoselov, and C. Casiraghi, Nano Lett. **12**, 617 (2012).
[32] M. Kalbac, A. Reina-Cecco, H. Farhat, J. Kong, L. Kavan, and M. S. Dresselhaus, ACS Nano **4**, 6055 (2010).
[33] D. M. Basko, S. Piscanec, and A. C. Ferrari, Phys. Rev. B **80**, 165413 (2009).
[34] C. Androulidakis, E. N. Koukaras, O. Frank, G. Tsoukleri, D. Sfyris, J. Parthenios, N. Pugno, K. Papagelis, K. S. Novoselov, and C. Galiotis, Sci. Rep. **4**, 5271 (2014).
[35] L. Gong, I. A. Kinloch, R. J. Young, I. Riaz, R. Jalil, and K. S. Novoselov, Adv. Mater. **22**, 2694 (2010).
[36] G. Anagnostopoulos, C. Androulidakis, E. N. Koukaras, G. Tsoukleri, I. Polyzos, J. Parthenios, K. Papagelis, and C. Galiotis, ACS Appl. Mater. Interfaces **7**, 4216 (2015).
[37] Z. Li, I. A. Kinloch, R. J. Young, K. S. Novoselov, G. Anagnostopoulos, J. Parthenios, C. Galiotis, K. Papagelis, C.-Y. Lu, and L. Britnell, ACS Nano **9**, 3917 (2015).
[38] S. Jegal, Y. Hao, D. Yoon, R. S. Ruoff, H. Yun, S. W. Lee, and H. Cheong, Chem. Phys. Lett. **568–569**, 146 (2013).
[39] J. Ek-Weis, S. Costa, O. Frank, and M. Kalbac, J. Phys. Chem. Lett. **5**, 549 (2014).
[40] J. Song, F.-Y. Kam, R.-Q. Png, W.-L. Seah, J.-M. Zhuo, G.-K. Lim, P. K. H. Ho, and L.-L. Chua, Nature Nanotechnol. **8**, 356 (2013).
[41] A. P. A. Raju, A. Lewis, B. Derby, R. J. Young, I. A. Kinloch, R. Zan, and K. S. Novoselov, Adv. Funct. Mater. **24**, 2865 (2014).
[42] R. Jalilian, L. A. Jauregui, G. Lopez, J. Tian, C. Roecker, M. M. Yazdanpanah, R. W. Cohn, I. Jovanovic, and Y. P. Chen, Nanotechnology **22**, 295705 (2011).
[43] R. Beams, L. Gustavo Cancado, and L. Novotny, J. Phys.: Condens. Matter **27**, 083002 (2015).
[44] C. Neumann, S. Reichardt, P. Venezuela, M. Drogeler, L. Banszerus, M. Schmitz, K. Watanabe, T. Taniguchi, F. Mauri, B. Beschoten, S. V. Rotkin, and C. Stampfer, Nature Commun. **6**, 8429 (2015).

© 2016 WILEY-VCH Verlag GmbH & Co. KGaA, Weinheim